Assessment of Environments for Mars Science Laboratory Entry, Descent, and Surface Operations

Ashwin R. Vasavada · Allen Chen · Jeffrey R. Barnes · P. Daniel Burkhart · Bruce A. Cantor · Alicia M. Dwyer-Cianciolo · Robin L. Fergason · David P. Hinson · Hilary L. Justh · David M. Kass · Stephen R. Lewis · Michael A. Mischna · James R. Murphy · Scot C.R. Rafkin · Daniel Tyler · Paul G. Withers

Abstract The Mars Science Laboratory mission aims to land a car-sized rover on Mars' surface and operate it for at least one Mars year in order to assess whether its field area

A.R. Vasavada (✉) · A. Chen · P.D. Burkhart · D.M. Kass · M.A. Mischna
Jet Propulsion Laboratory, California Institute of Technology, 4800 Oak Grove Drive, Pasadena, CA 91109, USA
e-mail: ashwin@jpl.nasa.gov

J.R. Barnes · D. Tyler
Oregon State University, Corvallis, OR, USA

B.A. Cantor
Malin Space Science Systems, San Diego, CA, USA

A.M. Dwyer-Cianciolo
NASA Langley Research Center, Hampton, VA, USA

R.L. Fergason
United States Geological Survey, Flagstaff, AZ, USA

D.P. Hinson
SETI Institute, Mountain View, CA, USA

H.L. Justh
NASA Marshall Space Flight Center, Huntsville, AL, USA

S.R. Lewis
The Open University, Milton Keynes, UK

J.R. Murphy
New Mexico State University, Las Cruces, NM, USA

S.C.R. Rafkin
Southwest Research Institute, Boulder, CO, USA

P.G. Withers
Boston University, Boston, MA, USA

was ever capable of supporting microbial life. Here we describe the approach used to identify, characterize, and assess environmental risks to the landing and rover surface operations. Novel entry, descent, and landing approaches will be used to accurately deliver the 900-kg rover, including the ability to sense and "fly out" deviations from a best-estimate atmospheric state. A joint engineering and science team developed methods to estimate the range of potential atmospheric states at the time of arrival and to quantitatively assess the spacecraft's performance and risk given its particular sensitivities to atmospheric conditions. Numerical models are used to calculate the atmospheric parameters, with observations used to define model cases, tune model parameters, and validate results. This joint program has resulted in a spacecraft capable of accessing, with minimal risk, the four finalist sites chosen for their scientific merit. The capability to operate the landed rover over the latitude range of candidate landing sites, and for all seasons, was verified against an analysis of surface environmental conditions described here. These results, from orbital and model data sets, also drive engineering simulations of the rover's thermal state that are used to plan surface operations.

Keywords Mars · Mars' atmosphere · Mars' surface · Spacecraft

Abbreviations

AGL	Above Ground Level
EDL	Entry, Descent, and Landing
GFDL	Geophysical Fluid Dynamics Laboratory, Princeton University
IR	Infrared
JPL	Jet Propulsion Laboratory
MARCI	Mars Color Imager
Mars-GRAM	Mars Global Reference Atmospheric Model
MCS	Mars Climate Sounder
MEP	Mars Exploration Program
MER	Mars Exploration Rover
MGCM	Mars General Circulation Model
MGS	Mars Global Surveyor
MOC	Mars Orbiter Camera
MOLA	Mars Orbiter Laser Altimeter
MMM5	Mars Mesoscale Model 5
MPF	Mars Pathfinder
MRAMS	Mars Regional Atmospheric Modeling System
MRO	Mars Reconnaissance Orbiter
MSL	Mars Science Laboratory
MY	Mars Year
NASA	National Aeronautics and Space Administration
NMSU	New Mexico State University
ODY	Mars Odyssey
RS	Radio Science
TES	Thermal Emission Spectrometer
THEMIS	Thermal Emission Imaging System
UKMGCM	United Kingdom MGCM
UTC	Coordinated Universal Time
VL	Viking Lander

1 Introduction

From its inception, the MSL mission has been designed to make fundamental advancements in NASA's capability to explore Mars, both scientifically and technologically. Key goals are to deliver an analytical laboratory payload to Mars' surface, to acquire and analyze many samples of rock and soil with the laboratory, and to conduct investigations over at least one Mars year in a location that may contain evidence of habitable environments in Mars' past, i.e., those capable of supporting microbial life (Grotzinger et al. 2012; Grotzinger 2009). Meeting these high-level goals required an EDL system capable of delivering a larger and more massive rover than any previous mission, and landing it more accurately than any previous mission (decreasing the size of the smooth, flat areas needed for landing in order to open more of Mars' surface to site selection). The selection of the final landing site was deliberately delayed until late in the rover's development, to allow more time for the scientific study of candidate sites from orbital data sets (Grant et al. 2011; Golombek et al. 2012). Therefore the system's design needed to accommodate the wide range of latitudes and elevations of any potential sites. Finally, the rover system needed the mobility and life expectancy to explore a broad region, requiring the capability to survive and operate over the wide range of environmental conditions that occur across the potential sites.

While the quantitative targets for these goals evolved during the design and development phase of MSL (Golombek et al. 2012), the final top-level requirements called for a rover mass of 900 kg (compared with 180 kg for the MER rovers), a latitude range of $\pm 30°$ (15°S to 10°N for MER), an elevation limit of $< +1$ km relative to the MGS-MOLA areoid (< -1.3 km for MER), a 3-sigma (99.87 %) landing uncertainty bounded by an ellipse of 25×20 km (80×10 km for MER-A, 115×12 km for MER-B), and a design lifetime of one Mars year, or 667 diurnal cycles (667 sols; compared with 90 sols for MER). The field of potential landing sites was narrowed in 2008 to four finalists (Table 1) that remained in study until just four months before launch. In July 2011 NASA announced the selection of Gale crater as the landing site for MSL, with arrival on 6 August 2012 (UTC), corresponding to $L_s = 150.7°$ on Mars (just before southern spring equinox). Entry occurs near 3:30 pm local true solar time on Mars (near 3 pm local mean solar time).

To design and validate the EDL and rover systems, the engineering teams needed accurate characterizations of the atmospheric and surface environmental conditions, as well as the characteristics of the terrain. In 2006, the MSL Project chartered a working group consisting of the core EDL engineers along with Mars atmospheric scientists from JPL and other institutions, some of whom were selected and funded through NASA's MEP Critical Data Products program. This working group, informally called the MSL Council of Atmospheres, jointly developed an understanding of the sensitivities of the EDL system to atmospheric variables such as density, wind, and dust. It also gathered observational data to characterize the atmosphere globally and at candidate landing sites, and defined a numerical modeling campaign. The results of these models, which were validated against observational data, were delivered as inputs for the engineering simulations used to assess EDL performance

Table 1 Finalist landing site candidates

Landing Site	Latitude	Longitude	Elevation (m)
Eberswalde	23.90°S	326.74°E	−1435
Gale Crater	4.49°S	137.42°E	−4444
Holden Crater	26.40°S	325.16°E	−2177
Mawrth Vallis	23.99°N	341.04°E	−2245

Fig. 1 Major spacecraft
components of the Mars Science
Laboratory. The Bridle Umbilical
Device (BUD) is the system of
three tethers and data cable, and
the mechanisms that extend them
during the sky crane events
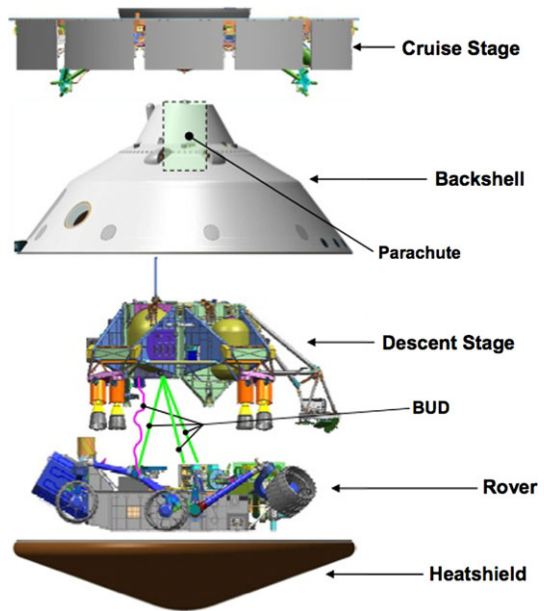
and risk. Sections 2–5 of this paper describe the characterization program that provided
these EDL-specific data to the MSL Project, and its major results. Section 6 describes the
work to characterize the surface environments relevant to the one-Mars-year primary mis-
sion. This work was completed by a smaller team consisting of the lead author, Jim Murphy
of NMSU, and Robin Fergason of the United States Geological Survey in Flagstaff. A com-
panion paper discusses the characterization of the terrain, along with the scientific merits of
candidate landing sites (Golombek et al. 2012).

2 Overview of EDL Design

The MSL rover, Curiosity, journeys to Mars attached to its rocket-powered descent stage,
with its wheels and suspension system retracted toward its chassis (Fig. 1). These are en-
closed within a 4.5-m diameter aeroshell and heat shield, forming the atmospheric entry
vehicle. The entry vehicle is escorted to Mars by a cruise stage, which supplies solar elec-
trical power, communications, and navigation between Earth and Mars, and is jettisoned
before atmospheric entry. The EDL sequence of events is illustrated in Fig. 2.

The challenging requirements described in Sect. 1 led to several novel approaches in
the MSL EDL design (Prakash et al. 2008). Delivering a heavy rover to higher elevations
than previous missions required enhancing the deceleration in the thin Martian atmosphere.
Options involving multiple parachute stages and retro rockets were studied, but ultimately
an approach was taken that uses the entry vehicle to generate lift. Prior to atmospheric
entry, balance masses are jettisoned from the aeroshell, displacing its center of mass from
its spin-balanced state during cruise. Once in the atmosphere, this results in an 18–24° angle
of attack that can be oriented using rocket thrusters. The vehicle generates enough lift to
maintain nearly level flight over a horizontal distance of about 100 km at an altitude of
about 10–15 km, providing extra time to decelerate and increasing the altitude of parachute
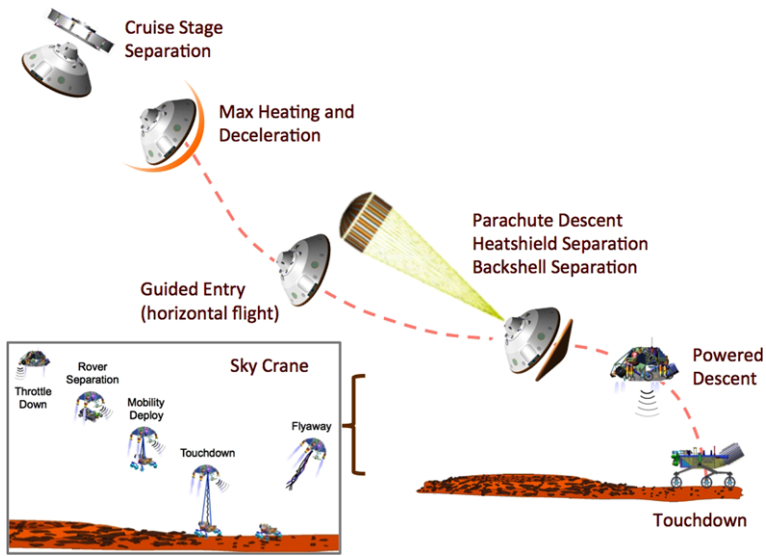deployment relative to a ballistic trajectory.

Fig. 2 Cartoon of the major events of entry, descent, and landing

Another novel approach, used to improve landing accuracy, also occurs during the entry phase of the flight. MSL has the ability to orient its lift vector, providing a "control stick" that is used to steer out deviations from an ideal flight path caused by the known error in the atmospheric entry point, atmospheric density and wind anomalies, and aerodynamic performance (as measured by onboard accelerometers). This Apollo-derived, closed-loop control scheme, called guided entry, greatly improves the along-track accuracy of landing, resulting in a near-circular landing uncertainty ellipse instead of the narrow and long ellipses in previous missions. Additional balance masses are jettisoned to remove the angle of attack and a 21.5-m parachute is deployed, further decelerating the spacecraft to $\sim$100 m s^{-1} and changing its direction of flight close to vertical. During parachute descent, the heat shield is jettisoned and the descent stage begins using a 6-beam radar system to sense altitude and velocity with respect to the surface.

A third novel aspect of MSL EDL is the method of final descent and touchdown. With a MER-like airbag system infeasible due to the mass of Curiosity, engineers considered landing the rover on a rocket-powered platform (essentially a legged lander like Viking, but with the rover on top). However, the platform required to absorb the touchdown of the 900-kg rover would itself require considerable mass. And, there is risk to the rover during egress from a raised platform. The solution was to fly the rover to the surface using a rocket-powered descent module, but to keep this module *above* the rover during touchdown, much like a helicopter setting down a suspended load of cargo. The rover would serve as its own landing platform by absorbing the impact within its suspension system, leaving the rover with its wheels on Martian soil. The "sky crane" system has other additional benefits. By keeping the rocket motors >8 m from the surface, interactions with the surface are lessened, allowing closed-loop control to be maintained and decreasing excavation of dust or rocks. Robustly identifying the dynamic touchdown event has proven tricky on previous missions, but on MSL it is seen as a persistent change in the throttle setting, as the ground takes up the rover's weight.

Returning to the EDL timeline, at an altitude of 1.5 to 2 km AGL (depending on the radar-derived altitude and velocity) and a velocity near $100 \, \mathrm{m \, s^{-1}}$, the descent stage and attached rover disconnect from the parachute and aeroshell, and begin a final deceleration and descent to the surface under the power of eight rocket motors. Just over 18 m above the surface, the sky crane maneuver begins. As the joint system continues to descend vertically at $0.75 \, \mathrm{m \, s^{-1}}$, the rover is lowered on three 7.5-m bridles (and a data umbilical) while the suspension and wheels deploy. Upon sensing touchdown, the bridles are cut at the rover and the descent stage powers up and flies away using its remaining fuel. The final uncertainty in the location of landing (a 3-sigma landing uncertainty bounded by an ellipse of 25×20 km) reflects the error in attitude at the time of cruise stage separation, the uncertainty in the spacecraft's knowledge of its position and velocity at the atmospheric entry point, and the error accumulated by drift due to winds while on the parachute.

3 Introduction to EDL Atmospheric Safety Assessment

3.1 Sensitivities of the EDL System to Atmospheric Conditions

A critical component of the risk assessment of each landing site is the analysis of the EDL system performance against expected local atmospheric characteristics. The dominant parameter is atmospheric density, or perhaps more accurately, the integrated stopping power of the atmosphere above any particular site given its elevation and the details of the EDL system. As described in Golombek et al. (2012), the initial elevation design goal of $+2.5$ km was chosen to allow access to more of Mars' surface, but was lowered over time as the list of candidate sites narrowed and need for elevations >0 km disappeared. Other characteristics that affect the performance of the EDL system are density variability and wind (magnitude, direction, and variability over a range of length and temporal scales). The various stages of EDL such as encapsulated flight, parachute deployment, parachute descent, and powered descent, all have different vulnerabilities to these parameters, so each must be evaluated at the relevant altitude and horizontal range from the landing target. The unique trajectory and architecture for MSL result in atmospheric sensitivities different from past missions (Chen et al. 2010). For example, due to the guided entry, MSL studies cannot rely only upon vertical profiles above the sites, but must also consider the conditions over 100 km up range from the site.

Identifying these sensitivities instructs the team where to focus their system performance studies and efforts to collect and analyze atmospheric data. The entry phase occurs at velocities of thousands to hundreds of $\mathrm{m \, s^{-1}}$ and therefore is tolerant to the expected uncertainties in density and wind speed at altitudes >30 km. Guided entry involves nearly level flight for ~100 km at an elevation of 10–15 km altitude, introducing a strong sensitivity to the density there (and its variability and uncertainty). During this phase, the spacecraft controls its altitude to seek the optimal density-driven deceleration, using algorithms that incorporate a temporal filter. Certain scales of density fluctuations could resonate with the system in undesirable ways. The EDL team simulated flights through the atmosphere with density "speed bumps" (local increases) and "potholes" (local decreases) of various magnitudes and spatial scales to assess this effect (Cianciolo et al. 2008a). Density variations driven by gravity waves are considered the largest threat, but it was determined that the EDL system is robust to the scales of fluctuations that might be present in the Martian atmosphere (e.g., up to 30 % variations in density over horizontal scales of 10 to 100 s of km).

Just prior to parachute deployment, the EDL system becomes limited in its ability to control for downrange distance. Any density or wind differences from predictions directly

impact landing accuracy and the safety margin in elevation. The parachute deployment event and the heat shield jettison event both are triggered at certain inertially navigated velocities, as calculated by propagating the initial entry velocity using onboard accelerometers. Deviations from predicted winds at the times of these triggers can cause the calculated velocities and true airspeeds to differ, resulting in sub-optimal performance and increased risk to a successful EDL.

The parachute is used for deceleration and will bring the system to near terminal velocity. While on the parachute, winds can cause the spacecraft to drift from its intended target. Accounting for uncertainty in wind direction and magnitude in the final landing error ellipse helps to ensure that there is no associated safety threat. The parachute phase ends when the spacecraft computes (using accelerometers) that it has reached the optimal velocity and altitude to initiate powered descent. The powered descent phase is complex due to the many events that must occur within the final ∼2 minutes of flight, such as sensing the surface with the radar and decelerating to the rover separation velocity, and the need to reach the surface with sufficient fuel. Uncertainty in vertical winds at the initiation of powered descent is a key risk factor due to its direct relationship to timing uncertainty. However the subsequent powered descent and sky crane phases of EDL are relatively immune to variations in density and wind (including turbulence), due to the mass of the spacecraft and their powered flight.

3.2 Approach to EDL Atmospheric Safety Assessment

The safety assessment of potential landing sites was a Project-led activity run in parallel with the landing site selection campaign that was open to scientists around the world. That campaign and the risk assessment against terrain-related characteristics, such as slopes and rock abundance, are described in Golombek et al. (2012). This section describes the Project's approach to assessing risk against atmospheric characteristics. To characterize the performance of the MSL EDL system, reveal its sensitivities, and quantify the risk to the mission, we must first develop an understanding of the plausible range of atmospheric conditions expected at the time and season of arrival. This understanding will include the best prediction of a mean state, a measure of the variability around that state, and an estimate of the uncertainty in our knowledge.

In the early stages of site selection, the EDL team compiled a list of acceptable values for atmospheric parameters based on their initial estimates of system sensitivities (Table 2). This list was distributed in 2006 to the site selection community, who used it to vet potential sites by examining existing orbital and model data sets. Certain sites were determined to be risky if the atmospheric data exceeded certain thresholds, or if their proximity to topography (e.g., regional-scale features such as Syrtis or local canyon or crater walls) was judged to have a potential for strong winds or wind shears. Global-scale models were sufficient to judge the relative risk of various sites, guided by experience from the MER and Phoenix site selection analyses (Kass et al. 2003; Rafkin and Michaels 2003; Toigo and Richardson 2003; Tamppari et al. 2008; Tyler et al. 2008). Estimates of boundary layer thickness from these models were used as a proxy for the vigor of convective motions.

Once a smaller set of candidate sites was defined, the MSL Project chartered the Council of Atmospheres to define the atmospheric characteristics and their uncertainties at each site using high-resolution numerical models, and to integrate those results directly into EDL simulations. At this point, the threshold approach was dropped. Instead, Monte Carlo trajectory simulations, using a suite of plausible atmospheric states calculated by atmospheric numerical models, became the basis for validating the EDL approach and characterizing system margins (e.g., propellant, time, altitude, etc.). The group gathered historical statistics

Table 2 EDL atmospheric constraints circa 2007. Altitudes are relative to the MOLA-defined areoid except where noted to be Above Ground Level (AGL). The constraints are expressed as absolute values or the percentage uncertainty/variability (3-sigma). For altitudes above 8 km, the constraints must be met everywhere within 100 km of the landing site. Lower-altitude constraints must be met over an area tied to the landing accuracy (<10 km radial). There are additional constraints on latitude ($\pm45°$), elevation (<1 km), surface winds at all times of day and all seasons (<15 m s^{-1} steady and <30 m s^{-1} gusts), and a variety of terrain characteristics. EDL was predicted to occur at a Mars season of $L_s = 116$ to 128 and a Mars Local True Solar Time of 14:00 to 17:30

Altitude (km)	Density (unc.)	Horiz. wind (unc.)	Vert. wind unc.	m s^{-1}	Speed of sound (unc.)
20 to 30	<15 %				
8 to 20	<10 %	<25 %			<7 %
4 to 8		<20 %	<20 %		<7 %
1 to 5 AGL				<20	

of dust storms and other weather events that could cause rare but significant deviations from mean conditions, and ran additional models and EDL simulations for these atypical conditions. The atmospheric models were constrained by and validated against data sets from orbital imaging and sounding instruments (thermal and radio).

4 Inputs to EDL Atmospheric Safety Assessment

Our knowledge of Mars' atmosphere has increased dramatically since the Viking missions. Not only have orbiter missions provided global sounding and imaging of atmospheric phenomena, but topographic, albedo, and surface temperature data sets provide richly detailed boundary conditions for atmospheric studies. A few landed missions have contributed *in situ* measurements of pressure, winds, and radiative fluxes. Nevertheless, significant limitations remain. Most data sets have either sparse temporal or spatial coverage, or both. Sounding data have coarse spatial resolution and, with the exception of some radio science experiments (e.g., Hinson et al. 2008), fail to sample the critical planetary boundary layer. These limitations are magnified when one aims to observe and predict conditions at a km-scale location on Mars' surface. In order to provide the needed atmospheric characterization to the EDL team, the Council of Atmospheres assembled an array of complementary data sets and models.

4.1 Surface Pressure

As noted in Sect. 3, engineers assessing the performance of the EDL system are most concerned with the density encountered as a function of altitude. Atmospheric scientists, on the other hand, often conceive of atmospheric structure in terms of temperature as a function of pressure. The latter more naturally follows from the physical equations and is directly measured by thermal sounders. As demonstrated in the MER site selection process, temperature-pressure profiles generated by various atmospheric models may agree, indicating that their underlying physics is leading to the same outcome, while markedly disagreeing in their density-altitude profiles. The disagreement can largely be removed if the models are normalized to a common surface pressure. While not affecting the scientific results from these models, differences in the specification of total atmospheric mass (which controls surface pressure) may cause disagreements in density-altitude space. Consequently, we have

developed a method for more accurately bounding the surface pressure at the time, season, and location of EDL. If necessary, the various models used in the MSL assessment can be normalized to this benchmark surface pressure to ensure uniformity.

Exchange of CO_2 between the seasonal frost caps and the atmosphere results in a significant and repeatable cycle in total atmospheric mass. Total mass and surface pressure vary by ∼30 % over the year, resulting in significant variations in density at all altitudes as well. The VL provided a multiyear record of surface pressure at two locations, with the VL-1 record (22°N, −3.6 km) used most commonly to represent the global pressure cycle (Hess et al. 1980). The seasonal exchange of CO_2 is the dominant signal, but it is modulated by the effects of the geostrophic balance of the zonal winds, meridional circulations, baroclinic eddies, stationary waves, and thermal patterns. Diurnal-scale variations arise from thermal tides. The VL-1 record applies strictly to its particular elevation, location, and topographic context. MGCMs can be used to extend the VL-1 record to arbitrary locations and elevations, to the extent that the necessary physics are included and accurate. In addition, high-precision vertical profiles of pressure from radio occultations provide independent measurements at certain local times, seasons, and locations and can be used to validate the MGCM predictions (Hinson et al. 1999).

4.1.1 The UKMGCM

We chose the UKMGCM for our surface pressure predictions because of its reanalysis of MGS-TES temperature profiles over three annual cycles, resulting in more accurate global fields than model-only runs. The assimilation of MGS-TES data also allows investigation of interannual variability by inspecting the EDL season in three different past Mars years. The model has been calibrated against VL-1 pressure observations, validated against radio occultation profiles, and has the capability to interpolate surface pressures at model grid points to arbitrary locations on the highest-resolution degree MOLA topographic data set.

The UKMGCM employs spectral discretization of the geophysical fluid dynamics equations varying from a truncation at total spherical wavenumber 31 (denoted T31, roughly equivalent to a 3.75° latitude-longitude grid) to 170 (T170, roughly equivalent to a 0.70° degree grid). T31 was used for long-multiannual experiments with varying model parameters, with three Mars years simulated at T85 and focused periods of 50 days repeated at T127 and T170. The model has a finite-difference formulation in the vertical, spanning the range from the surface to about 95 km for the present set of experiments, and varying from 25 model levels for most experiments to 100 levels for some T31 sensitivity experiments. The lowest model level is about 4 m above the surface. Vertical spacing is ∼5 km above 25 km, with finer spacing below. Apart from the dynamical core and the data assimilation scheme, the UKMGCM uses the Laboratoire de Météorologie Dynamique MGCM physical parameterization schemes (Forget et al. 1999). These schemes include a 2.5-level Mellor-Yamada turbulence closure planetary boundary layer parameterization and enforce static stability with a dry convection scheme that ensures that the vertical gradient of potential temperature can never become negative.

In order to produce the most realistic atmospheric states for the MSL analysis, the UK-MGCM was constrained by data assimilation to produce a reanalysis of the three Mars years observed in detail by the MGS spacecraft during its scientific mapping phase. Data assimilation is the combination of observations and numerical models that provide physical constraints, organize and propagate the observational information, and enable the recovery of variables not directly measured. Data assimilation is commonly used as a means of analyzing large atmospheric and oceanic observational data sets for the Earth (e.g., Lahoz et al.

Fig. 3 Surface pressure predicted by the UKMGCM reanalysis for MY25 at the finalist landing sites around the time of MSL arrival ($L_s = 151°$). The *thin lines* show hourly pressures, while *thicker lines* show the diurnal-mean pressure, indicating the seasonal trend and any day-to-day variability (weather). There were no observations for a period of about two weeks centered on $L_s = 160°$, when the variability can be seen to reduce and become more regular
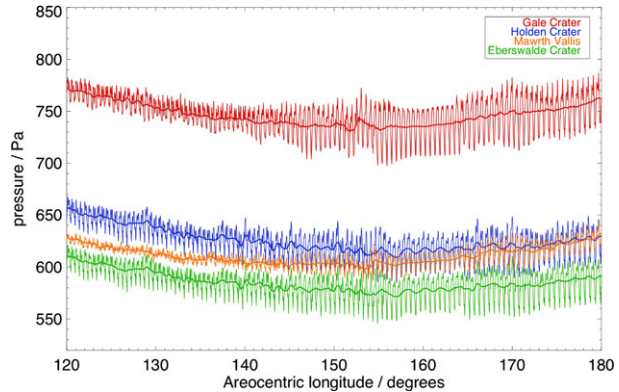

2010). The MGS-TES has produced an extensive atmospheric data set (Conrath et al. 2000; Smith 2004; Smith et al. 2000, 2001, 2002). MGS-TES spectra have permitted the retrieval of thermal profiles for the atmosphere, mainly from nadir soundings below about 40 km, and total atmospheric dust and water ice opacities. Assimilated MGS-TES data have been used to analyse atmospheric waves including the diurnal tide, semidiurnal tide and Kelvin mode (Lewis and Barker 2005), to investigate dust storms and atmospheric variability (Martinez-Alvarado et al. 2009) and predictability (Rogberg et al. 2010) and to identify model biases and errors, such as the neglect of water ice cloud radiative effects in the model used for initial assimilations (Wilson et al. 2008). These results have been validated against independent observations using radio occultation techniques (Montabone et al. 2006), a process which has continued as part of the current work. Assimilating MGS-TES data for the present work was seen as an advantage since the dataset is now well understood and the three Mars years of coverage provide the opportunity to analyze the MSL landing period with some element of interannual as well as day-to-day and diurnal variability. It is interesting to note that assimilations show more day-to-day variability than model-only simulations.

The MGS-TES reanalysis was produced following the scheme described by Lewis et al. (2007) by assimilating the MGS-TES temperature and column dust opacity retrievals into the UKMGCM to produce a physically self-consistent record of all atmospheric variables stored at a 1 or 2 hour interval over the entire MGS mapping period covering roughly three Mars years (Montabone et al. 2006). The assimilation was conducted using a modified form of the sequential Analysis Correction scheme (Lorenc et al. 1991) with parameters tuned for the specific case of Mars. Shorter, high-resolution (T127 and T170), assimilations were produced as sub-periods within the complete (T31 and T85) record, using initial states interpolated from the lower resolution model. In addition, UKMGCM control experiments were conducted using a matching prescribed dust state, but without assimilation of thermal data as a constraint. It is notable that the model-only simulations had less day-to-day variability than the full MGS reanalysis, a feature also observed during the reanalysis itself at times of solar conjunction when no spacecraft data were available (e.g., Fig. 3).

In order to interpolate results from the model grid to the high-resolution MGS-MOLA surface, the model temperature profile interpolated at the chosen time and location was used to integrate the hydrostatic equation in the vertical, and so to correct from the model surface pressure on the smoothed model surface to the predicted surface pressure on the MOLA topographic dataset. This process follows that developed by Forget et al. (2007) and used in more recent versions of the Mars Climate Database (Lewis et al. 1999), but here employs

Fig. 4 Comparison of the MY25 reanalysis (*curve*) with MRO-RS (*diamonds*) from MY 29 at the comparison site near Gale crater (5.0°S, 135.5°E, −1.136 km). The MRO-RS data were taken close to 0500 hr. The *small dots* mark the model pressures at that local time
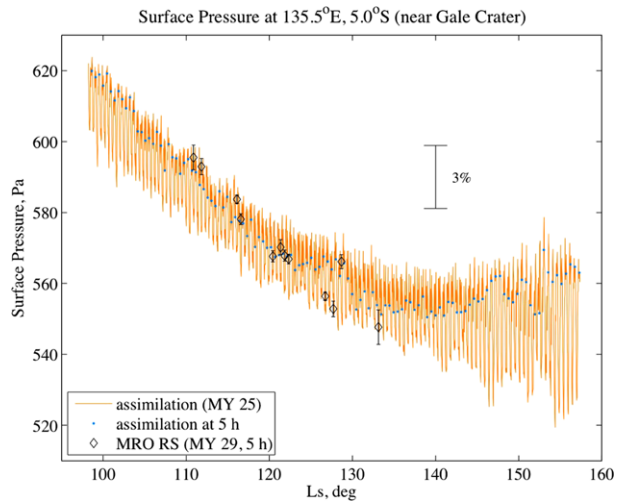
temperatures for each specific time and day rather than time-mean data. Generating T170-resolution equivalent surface pressure data from a T31 model and then comparing with a real T170 model validated the procedure. The UKMGCM reanalysis was calibrated against VL-1 surface pressure observations by predicting surface pressure at the VL-1 site and altitude, smoothing using a 30-day window to remove much of the weather that might differ from year-to-year, and comparing with real VL-1 observations, similarly smoothed with a 30-day window. Periods of major dust storms were removed from either data set. The VL-1 pressure tuning procedure largely followed the method used to tune model parameters described in Hourdin et al. (1995), but here provided a final correction to the global mean surface pressure of typically much less than 1 %, varying with time of year.

4.1.2 Surface Pressure Results

Figure 3 shows surface pressure predictions based on the reanalysis of MY25, but a similar period was analyzed for MY24 and MY26. (The Mars Year convention has MY1 starting in April 1955 at $L_s = 0$. MY24 began July 1998.) At the Gale crater site, each showed a growth in the amplitude of the diurnal cycle between $L_s = 140$–$150°$ and detailed differences in the small day-to-day variability. Focusing on the period around the MSL landing time, $L_s = 145$–$165°$, there were time-mean differences in surface pressure of about 10 Pa (1.3 %) between the lowest pressure in MY25 and the highest in MY26. These differences only arise as a result of changes in the thermal state of the model; the total CO_2 mass in the model is constrained by the VL observations as described above. There were also typical differences of order 10 Pa between each of the three years when comparing surface pressure at any single time as a result of variations in the amplitude of the diurnal cycle.

Our approach to predicting surface pressure was validated using RS data where available (e.g., http://www.lpi.usra.edu/meetings/sixthmars2003/pdf/3032.pdf). A site near Gale crater, but in a smoother region of terrain, was chosen for the comparison both to minimize the correction required for the reanalysis and to permit RS observations around the region to be combined, also without correction. Figure 4 shows the comparison between UKMGCM reanalysis predicted surface pressure and RS observed surface pressure at the comparison site, but from different MY (25 and 29 respectively), constrained by when the observations

were available. Results were found to agree to within about 1 %, once allowance was made for different weather in the two years.

As an additional check, we also used a simpler method based on traceability to observations of surface pressure, described by Withers (2012). He used landed (VL-1, VL-2, MPF, Phoenix) and orbital (MGS-RS) measurements of surface pressure to develop an empirical expression for the diurnal mean surface pressure. This expression assumed an exponential dependence on altitude with a scale height of 11 km and a harmonic dependence on season with annual and semi-annual terms. It was found to be accurate to 2 % (1-sigma) for the latitudes, seasons, and altitudes relevant for MSL landing sites. The predicted diurnal mean surface pressure at Gale crater at $L_s = 150°$ is 730 Pa, closely matching the UKMGCM result (Fig. 3).

4.2 Atmospheric Density

Two state-of-the-art Mars mesoscale models are used to calculate the detailed structure of the atmosphere (in density-altitude space) and its variability. Unlike previous missions with ballistic trajectories and large landing ellipses, MSL's horizontal flight will occur over large topographic variations outside of its smooth landing region. Topography-induced waves and winds, turbulence within the planetary boundary layer, and baroclinic eddies may introduce significant density variations along the incoming trajectory. Many of these phenomena cannot be resolved by MGCMs, but their impacts on EDL are important. This drives the need to explicitly resolve these circulations at higher resolution (∼km scale horizontally).

The Council of Atmospheres includes the primary model developers for both MRAMS, currently located at Southwest Research Institute, and the MMM5 model, developed by Oregon State University. While both use the NASA Ames MGCM for global boundary conditions, the mesoscale calculations are unique in terms of model architecture and coding. Both models perform calculations on a series of grids with increasing spatial resolution and decreasing domain size, with the output derived from the finest grid.

4.2.1 MRAMS

MRAMS was developed from a terrestrial weather model (Pielke et al. 1992) to investigate mesoscale and microscale processes within the atmosphere of Mars (e.g., Rafkin et al. 2001, 2002; Michaels and Rafkin 2004; Sta. Maria et al. 2006). MRAMS has been applied to provide guidance on the anticipated atmospheric environment during EDL for MER and all subsequent landed spacecraft (Rafkin et al. 2004; Rafkin and Michaels 2003; Michaels and Rafkin 2008). The application to MSL EDL follows the same basic methodology as for previous missions. The model remains very similar to that used for the Phoenix mission (Michaels and Rafkin 2008; Tamppari et al. 2008), although additional dust physics and dust simulation capabilities have since been added. These additional capabilities were used to investigate, for the first time on any mission, the impact of local and regional dust storms on spacecraft performance during EDL.

MRAMS is a sub-global model and must therefore be provided with initial and boundary conditions. The NASA Ames MGCM version 1.7.4 was used for this purpose (Kahre et al. 2006). Although the mesoscale simulations were integrated for nearly 30 sols, the solution, even deep within the interior of the mesoscale numerical domain, may be sensitive to both initial conditions and lateral boundary conditions. Therefore, it is important to utilize MGCM conditions that match as closely as possible the expected large-scale conditions. At the initiation of this project, thermal profiles and column dust opacity retrieved from MGS-TES provided the most valuable data set for MGCM comparison (Smith et al. 2001, 2002).
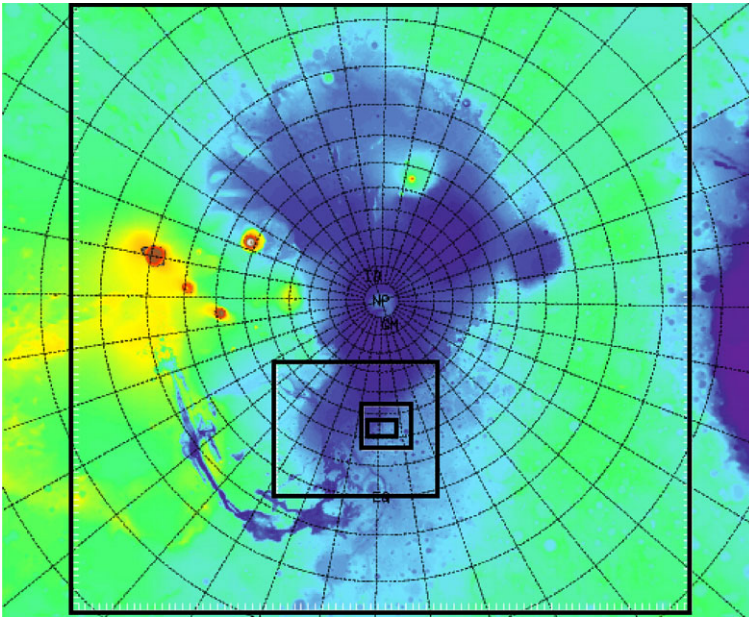
Fig. 5 MRAMS grid configuration, illustrating the two-way numerical grid nesting. The outermost mother domain is super-hemispheric in order to minimize numerical distortion of the propagating tropical thermal tide. In this example, additional grids telescope inward to the Mawrth Vallis landing site. Each successive grid has a spacing one-third as large as its parent. The mother domain has a grid spacing of 240 km at the pole. Grids 5 and 6 are not shown. The *background color* is MOLA surface elevation

A gridded data set derived from MGS-TES column opacity during years without planetary encircling dust storms was used to force the model. The primary adjustable parameter available for tuning the model to match the thermal profiles was the vertical distribution of dust. Two vertical dust distribution profiles were tested: Conrath-ν (Conrath 1975) and a haze top prescription (Forget et al. 1999). Despite a large number ($\sim$30) of MGCM simulations with differing vertical dust distributions, none was able to globally match MGS-TES temperature retrievals. Instead, the MGCM results showed that adjusting dust at one latitude to match TES temperatures resulted in poorer agreement at other latitudes. This suggests that either the assumptions about the vertical distribution of dust are not representative of reality or that the model physical parameterizations are deficient in some manner (or some combination of both). Recent observations by MRO-MCS strongly suggest that the actual dust vertical distribution is incompatible with Conrath-ν-like vertical distributions (Heavens et al. 2011; McCleese et al. 2010). In the end, the choice was made to utilize data from MGCM runs that minimized the overall temperature error. Dust scattering properties also affect the atmospheric temperature. The value used in MRAMS is derived from Mie scattering calculations assuming spherical palagonite particles.

MRAMS was configured similarly for all candidate landing sites. A super-hemispheric domain was centered on one of the poles. This domain extended well into the antipode hemisphere so that the tropical latitudes were contained completely with the domain. This configuration minimizes the potential for numerical distortions of the thermal tide that might occur if the waves have to propagate into and out of the grid (Tyler et al. 2002). Within this mother domain, additional two-way nested grids were focused on the landing site (Fig. 5).

The grid spacing of the mother domain was 240 km at the pole point. The Polar Stereographic projection used in the model means that the grid spacing is approximately half that at the equator. Additional nested grids consecutively reduced the grid spacing by a factor of three. Up to six grids were used resulting in a nominal horizontal spacing of ∼1 km on the last grid. The centers of the higher-resolution grids were typically shifted westward from the landing site to capture the upstream entry corridor of MSL. Vertical grid spacing was ∼10 m near the surface and was gradually stretched to a maximum of ∼5 km. The top of the model was at ∼65 km. Except for dust storm simulations, integrations with the first four nested grids were of 20–30 sols in duration, centered on the landing $L_s = 150°$. Due to the time required to run with grids 5 and 6, these high-resolution grids were added only for a few sols near $L_s = 150°$. Approximately two sols were required for the model to spin-up from the initial, coarse MGCM state.

Output from the MRAMS simulations was provided to the MSL project along with code to perform interpolation of the data in space and time. This code was used to extract atmospheric properties along a specified spacecraft entry trajectory. Model variables available within the data set included three-dimensional vector winds, pressure, temperature, and sub-grid scale turbulent kinetic energy. In the case of dust storm simulations, dust mixing ratio and column opacity were also provided. Because the atmosphere at the mesoscale and smaller scales is extremely dynamic during the afternoon when EDL is to occur, the model output was sampled over many times within the landing window over many model sols in order to generate a range of plausible entry profiles.

4.2.2 MMM5

The Oregon State University MMM5 is a mesoscale model developed from the Penn State/National Center for Atmospheric Research MM5 (Grell et al. 1994). The NASA Ames MGCM (Haberle et al. 1999) provides boundary and initial conditions for all model runs. Initial efforts compared model results to VL-1 and MPF surface observations (Tyler et al. 2002). The model was used in a comprehensive study of circulations in the Martian northern summer (Tyler and Barnes 2005), as well as in the EDL risk assessment for the Phoenix mission (Tyler et al. 2008).

The mother domain (lowest-resolution model grid and the one that uses MGCM boundary conditions) is Polar Stereographic and semi-global (the northern hemisphere case is shown in Fig. 6). Three levels of two-way nesting allow for very high horizontal resolution near landing sites (resolution increases three times with each level, so a third-level nest in a 135-km mother domain has a resolution of 5 km). In these studies a 55-layer vertical grid is used. Resolution near the ground is very good (center of the lowest layer is ∼5 m and most levels are in the lowest ∼20 km), and the resolution gradually decreases towards the model top at the 0.01 Pa pressure level. Model dynamics are hydrostatic and the length of all simulations is 30 sols. Nests are activated successively, the first after two sols, the second after four sols, and the third after six. The first ten sols are neglected due to model spin-up, and the final twenty (centered near the date of EDL, $L_s \sim 153°$) are used for analysis.

Since atmospheric dynamics are so strongly coupled to atmospheric thermal structure, an important part of this work was to compare and "tune" the model results to available observations. Using MGS-TES surface dust opacity data, zonal mean dust prescriptions were constructed. MRO-MCS atmospheric dust data (McCleese et al. 2010) were used to constrain the vertical dimension of the 2-D dust prescription (pressure versus latitude). Using MGS-TES and MRO-MCS temperature data, the dust prescription was adjusted so model temperatures agree with the nominal seasonal atmosphere (done iteratively with multiple
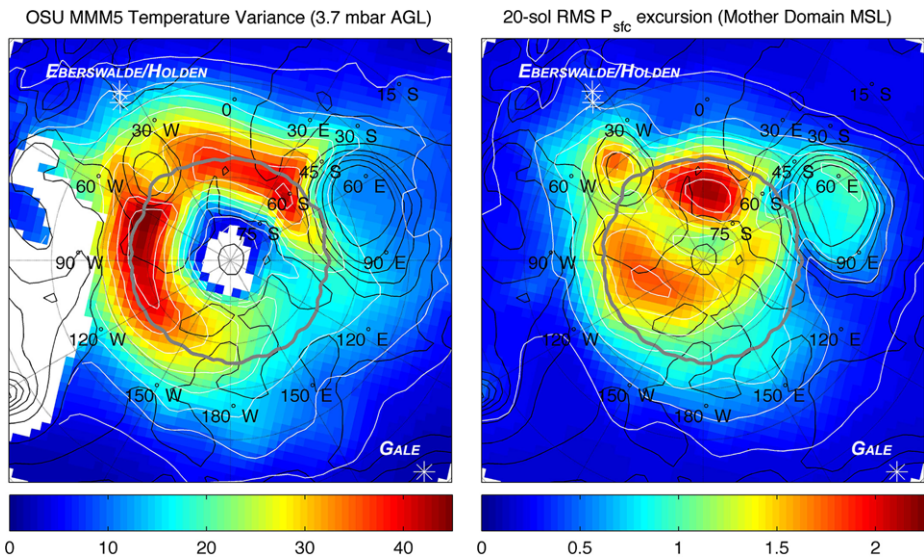
Fig. 6 MMM5 mother domain showing the twenty-sol mean of the model atmospheric temperature variance, K^2 (shown at MGS-TES level 7, $\sim$3.7 mbar) and the root mean square percentage of the surface pressure excursion calculated after Tyler and Barnes (2005), equations (6) and (7). The *gray line* marks the edge of the prescribed seasonal CO_2 cap edge at $L_s \sim 153°$ (Titus 2005) and the *black contours* show MGS-MOLA topography as used in the mother domain (1.5-km intervals)

MGCM runs). MGCM and mesoscale model predictions of the diurnal amplitudes of modeled atmospheric temperatures compare well with MRO-MCS observations.

Moreover, the MRO-MCS data motivated two questions that led to two parallel modeling studies: (1) the effects of the seasonally observed tropical dust mass mixing ratio maxima (that are seen aloft) on model results for MSL EDL, and (2) the importance of simulating the high-altitude polar warming observed by MRO-MCS (McCleese et al. 2008) for modeling the synoptic structure of winter transient eddies in the southern hemisphere circulation (for MSL prospective sites near 30°S). To examine the first question, a maximum in the tropical dust mass mixing ratios aloft was prescribed (guidance from N. Heavens, personal communication, 2009). This modification in itself did not yield significant changes in the model results, even when it was included in parallel with the second study. Regarding the importance of realistically simulating the polar warming, significant changes in the synoptic structure of the southern hemisphere winter storms were observed when the model polar warming is in better agreement with the MRO-MCS data.

Model representation of the polar warming (its amplitude and structure) is greatly improved with the inclusion of two changes (applied to both the MGCM and the mesoscale models): (1) a model top that is significantly raised to allow the high altitude large-scale subsidence to occur over the highest latitudes and produce the warming, and (2) a strong and deep Rayleigh Friction layer that varies in latitude (linear forcing to crudely represent the effect of breaking gravity waves). It is important to note that these changes at the top of the model result in significant change near the ground as well. The mean meridional circulation is modified and the zonal mean jet core forms nearer to the ground and nearer to the equator. The synoptic structure of transient winter storms is modified; they become stronger, with somewhat shorter zonal scales and are seen to migrate more rapidly. However, since the latitude of the storm zone is highly controlled by the location of the prescribed seasonal cap

Fig. 7 Depth of the convective
mixed layer, in km, near the Gale
crater landing site. These depths
are a mean over 1400–1600 hr
and twenty sols centered on EDL
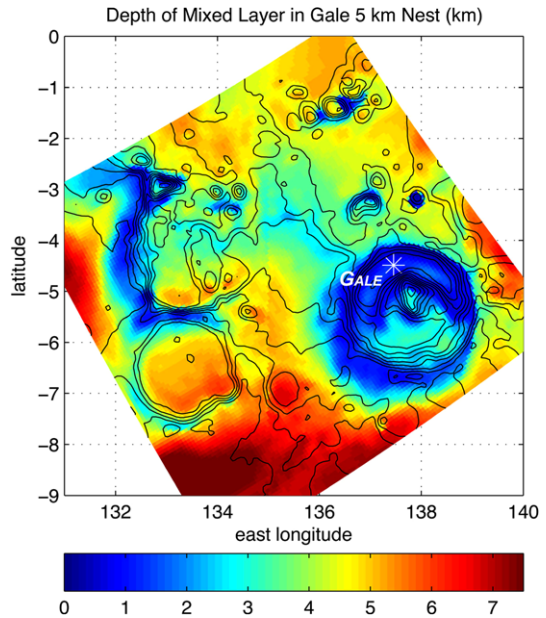
edge (based on Titus 2005), the EDL risk of a strong winter storm remains relatively small
at the southernmost finalist sites, Eberswalde and Holden crater. This is seen in Fig. 6, where
the 20-sol means for the modeled temperature variance and the RMS surface pressure excur-
sion from the diurnal surface pressure cycle (a good proxy for the strength and/or frequency
of storms) are shown for the southern-hemisphere mother domain. Although storm activ-
ity extends further equatorward in the vicinity of Argyre, it does not reach Eberswalde and
Holden with significant amplitudes. A favorable comparison (not shown) between modeled
temperature variance and that derived from MGS-TES observations (Barnes and Tyler 2007)
suggests that the synoptic structure depicted in Fig. 6 is realistic, especially the zonal asym-
metry. However, the modeled maximum variance amplitudes are ∼20 K^2 too small. These
results suggest some caution regarding the Eberswalde and Holden sites, but are within the
uncertainty assumed by the spacecraft team (Sect. 5). Some known model limitations re-
main, such as the inclusion of the radiative effects of water ice clouds.

Finally, as the MSL spacecraft nears parachute deployment, it has been flying horizon-
tally through the atmosphere at heights above the ground that are within the limits of the
deepest convection on Mars (Hinson et al. 2008). Since horizontal variations in topography,
albedo and thermal inertia produce a strong effect on the depth of the afternoon mixed layer
(the vertical depth of thermal convection), it was important to examine whether the space-
craft might be performing its final EDL trajectory corrections in the turbulence and wind
shears that are expected in the atmosphere near the top of the convective mixed layer. For
Gale, a map of the mean depth of the mixed layer during the local time window of 1400–
1600 hr is shown in Fig. 7. Mixed-layer depth is defined as the altitude (AGL) at which there
is a secular change in the slope of potential temperature with height, from being constant
with height to increasing with height. This shows that, for MSL EDL at Gale, horizontal
flight at ∼10+ km AGL is safely above the turbulent mixed layer at the local solar time of
EDL.

4.3 Winds

As described earlier, both horizontal and vertical winds, and their variability, affect EDL performance. Winds can be driven by planetary circulations, mesoscale disturbances, local topography, and convection. The MGCM-bounded mesoscale models are capable of simulating these processes, though the smallest scale convective activity within the boundary layer is parameterized. Planetary-scale circulations can be inferred from the thermal structure and share similarities to jet streams and meridional circulations on Earth. But knowledge of the winds within the first few km of the surface, as driven by topography and surface heating, is very limited. Further, convective boundary layer processes are known to differ from those on Earth due to Mars' thin, dry atmosphere. Consequently, the vertical winds and turbulence in the boundary layer are estimated from theory and large eddy simulations, but the MSL safety assessment (Sect. 5) allows for large error in these predictions.

Equatorial sites, such as Gale crater, are especially challenging, since the Coriolis force vanishes at the equator. Other terms in the model physics and dynamics dominate the force balance, where the relationships are highly nonlinear. Careful model inter-comparison studies increase our confidence. However, *in situ* observations of the diurnal cycle of winds and temperature in the lowest pressure scale height are sorely needed (and some relevant data will come the MSL meteorology instrument).

4.3.1 Winds at Gale Crater

Gale crater sits on the Martian dichotomy boundary, where the southern highlands drop steeply into the northern lowlands. This large-scale topographic gradient causes strong down-slope katabatic winds to develop at night. After sunrise, as solar heating warms the ground, winds near the surface rotate into the up-slope direction. The topography of the Gale crater region is complex, with significant relief even in comparison to the regional changes in elevation along the dichotomy boundary. When the regional variations in albedo and thermal inertia also are considered, we expect a large spatial and temporal variability in the diurnal wind cycle. This is seen in mesoscale model results; an example of morning surface winds from the MMM5 is shown in Fig. 8a. The steepest slopes can have surface winds in excess of 25 m s^{-1}. One "channel" of the regional katabatic flow is evident just west of Gale crater.

By the afternoon time of EDL, the convective mixed layer is nearing its maximum daily depth. The greatest depths occur over the higher topography to the south-southwest of Gale crater (Fig. 7). Inside large and deep craters, the mixed layer depths can be much smaller due to crater circulations, where up-slope flow at crater walls requires subsidence in the interior of the crater to conserve mass, and due to the greater surface pressure (Hinson et al. 2008; Spiga et al. 2010). An example from the MMM5 is shown in Fig. 8b. Fixed convective plumes form over many of the hills. Examination of the wind field suggests that open-cell convection is involved in forming the deeper mixed layers, such as in the higher elevations to the southwest of Gale crater, where the mixed layers are ∼8 km. Wind vectors that are coincident with the largest vertical velocities show the near-surface convergence that is responsible for the formation of transient open-cell structures. Our mesoscale simulations resolve only the large end of the expected range of eddy length scales. At the time of EDL, surface winds at the Gale crater landing site are mostly calm in the MMM5. MRAMS runs at higher resolution with non-hydrostatic dynamics over Gale crater and predicts a similar wind environment.

During EDL, when the spacecraft is decelerating in horizontal flight (∼10–15 km AGL), large errors in the predicted winds aloft could affect the MSL spacecraft performance and

Fig. 8 Winds at Gale crater.
(**a**) Morning surface winds
(∼5 m AGL, every other grid
point) from the MMM5 are
shown on topography. The *white
marker* is the center of the
landing ellipse in Gale crater.
The *grey lines* are contours of
MGS-MOLA topography for the
model nest (resolution of
∼5 km). (**b**) Afternoon
near-surface winds (∼45 m AGL,
every other grid point) are shown
on vertical velocity (*color*) at a
mean height of ∼3.3 km AGL.
The *white marker* is the center of
the landing ellipse. The *grey lines*
are contours of MGS-MOLA
topography for the model nest
(resolution of ∼5 km)

(a)

(b)
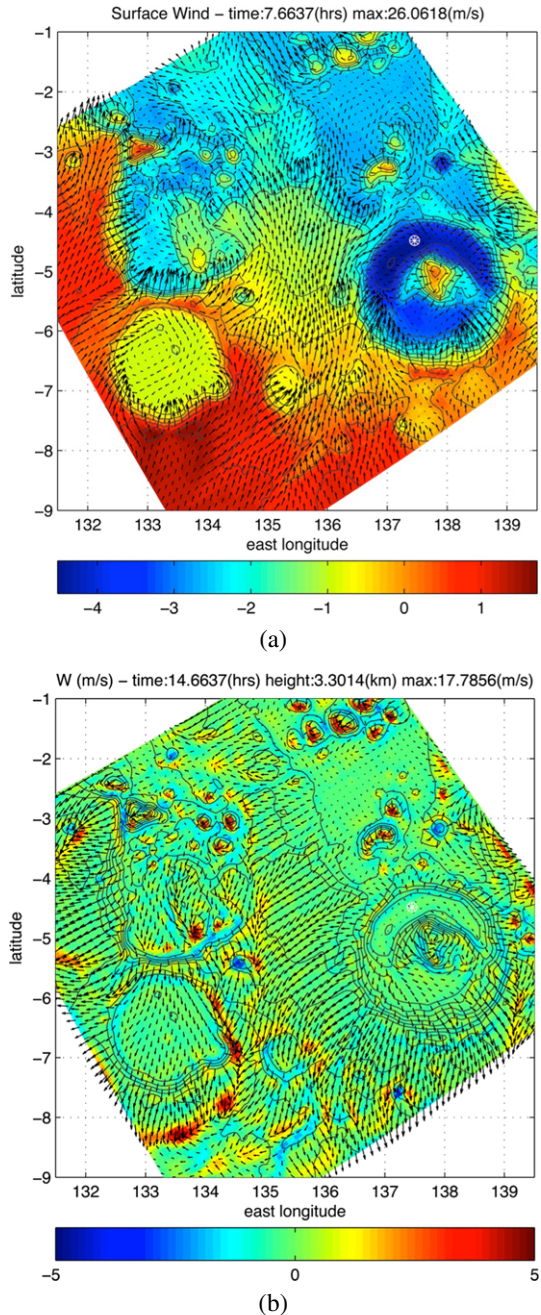
landing accuracy. Modeled winds aloft exhibit much less horizontal structure than winds near the surface. The MMM5 predicts weak (∼5 m s^{-1}) winds aloft at the time of EDL near Gale crater. Late morning winds aloft are quite uniform in the MMM5 (from the south-southeast with speeds of ∼10 m s^{-1}). Through afternoon and into the early evening, winds aloft weaken, and on average rotate to a westerly direction. The maximum wind speeds aloft

reach $\sim$15 m s^{-1} shortly after midnight before the winds weaken and rotate back to the late morning direction shortly after sunrise.

4.4 Dust Events

While using the models and methods described above to address the nominal range of atmospheric conditions for EDL, the team also investigated the effects of transient atmospheric phenomena, the most likely being dust events (at these latitudes and season). Dust storms can affect the atmospheric density structure and winds, though their specific effects vary with location and season. Enhanced atmospheric dust loading typically causes strong diurnal radiative forcing of atmospheric temperature through enhanced heating/cooling during the day/night.

To assess the likelihood of dust events at the candidate landing sites and to characterize those events, the team used data from MGS-MOC and MRO-MARCI. A survey of dust events near the finalist landing sites has revealed the size, opacity, and frequency of the events (dominated by short-lived, local dust storms). Because of the difficulty in finding thermal sounding measurements that capture these storms (and due to the lack of wind measurements in general), these observed parameters were used to define a number of MRAMS and MMM5 model runs to understand the resulting effects on density and winds. Starting with MMM5, the approach was to force a dust distribution similar to what was observed. This method has the advantage of ensuring a known and appropriate size, location, and temporal evolution of the dust events, but has the disadvantage that the winds do not feed back to the dust distribution. The MRAMS model allowed dust storms to form organically by adjusting dust-lifting efficiencies. This had the advantage of producing a storm consistent with the dynamics, with the dust and wind fields evolving consistently. The disadvantage is that the size, location, intensity, and evolution are not constrained to the observations. Given the complementary nature of these approaches, we decided to explore both.

4.4.1 Dust Events as Derived from Orbital Observations

The MSL landing occurs earlier in the Martian year than the 'dusty' southern hemisphere summer season. Planetary-scale dust events are not expected during MSL EDL; however, local-to-regional scale dust storms have been observed near this season and can influence the local atmosphere. The probability of encountering such events during EDL at the four finalist MSL landing sites was explored through a statistical study of past local dust storm occurrence and location.

To establish dust storm frequency, a monitoring region of 40° latitude by 60° longitude was centered on each finalist landing site. The number of dust storms observed in this region and within a seasonal window of $L_s = 140$–170° was tallied for each site. Dust storm data were acquired from regular observations by the MGS-MOC and MRO-MARCI cameras, spanning six Mars years (MY24-29), from 1999 to 2008. The number of observed local dust storms across the four sites varied greatly (Fig. 9), from 12 storms within the Gale crater monitoring region, to 329 storms for Holden crater.

Several simplifying approximations to dust storm behavior were made to compute the probability of encounter: a fixed dust storm size (500-km diameter) and duration (2 sols), and an equal likelihood of MSL landing at any location within the monitoring region. Results indicate a very small probability of encounter regardless of landing site, with all locations having a probability of <3 %, and the chosen landing site, Gale crater, having a probability of $\sim$0.1 %. Local dust storms are quite uncommon near Gale crater during this season
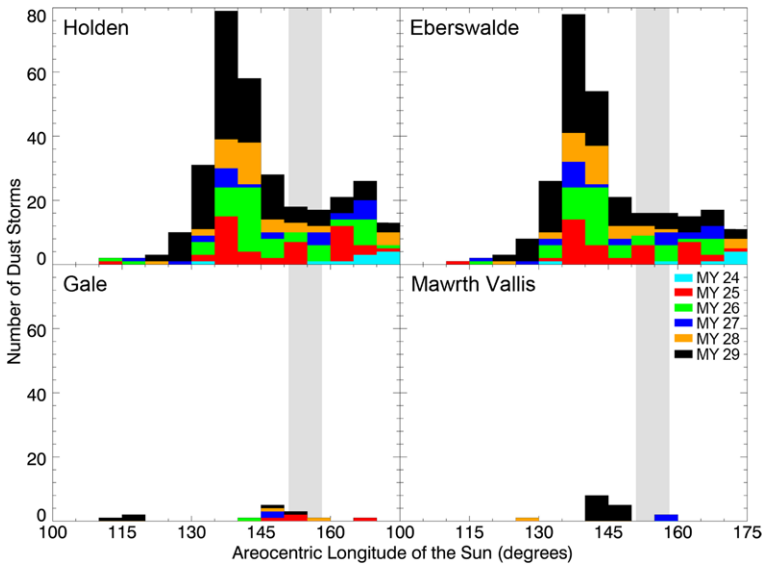
Fig. 9 Histogram of the number of local dust storms at the four finalist landing sites between $L_S = 100–175°$. *Colored bars* represent individual Mars years. The *gray region* in each plot marks the $L_s = 151–158°$ landing season considered for MSL at the time of the study

(Fig. 9). Even these low probabilities are quite conservative for Eberswalde and Holden, given that the large study region includes higher southern latitudes (where storms are more frequent), and the seasonal window includes non-relevant portions when many storms occur (e.g., $L_s = 135–145°$).

4.4.2 MMM5 Dusty Simulations

Using observationally informed guidance for the lifetime, opacity, horizontal size, and vertical depth of characteristic dust storms (M. Smith and B. Cantor, personal communication, 2009), numerous dust storm scenarios were prescribed in MMM5. Both small, short-lived local storms and much larger, multi-sol regional storms were examined, first focusing on the Mawrth Vallis site because of its higher insolation at the time of EDL. The small storm simulations used a 500-km diameter with an opacity that faded radially from a maximum at the center. Other experiments assumed sharper edges and storms with diameters up to 750 km. Visible opacities (at the ground) for these storms were ∼1.5 (500 km storms) and up to ∼2.5 (750 km storms). These stationary "dust bombs" were prescribed to last only a few sols, ramping up fast and fading more slowly. This diagnostic approach (a prescribed storm) is highly complementary to that used with MRAMS (below), yielding similar density, temperature and wind excursion amplitudes when sharp edges are prescribed for the dust storm.

Another experiment, carried out at all the finalist sites, allowed the prescribed storms to translate. These "dust bombs" grew radially, with maximum storm cores of 750 km with sharp edges (maximum opacity of ∼3), surrounded by a dust haze ∼2000 km in longitude and ∼1000 km in latitude. The quick growth and gradual fade to the background dust environment evolved over a total of 10 sols. In order to provide an upper bound on the thermal forcing, experiments were run for Holden crater and Mawrth Vallis using large cores, opacities of ∼3.5, with very sharp edges. Figure 10 shows the results of a "direct hit" dust storm

Fig. 10 Column dust opacity for a dust storm, prescribed in both time and space, that reached maximum opacity as it crossed over the Mawrth Vallis landing site. The MGS-MOLA topography of the mother domain is shown with *gray contour lines*. The most opaque central part of the prescribed storm has a very sharp edge, whereas the prescribed "haze" surrounding the center fades gradually into the background dust prescription
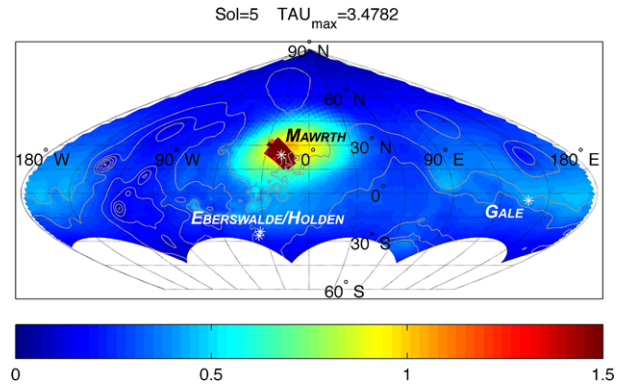
examined with MMM5. For a quantitative analysis and comparison with the no-dust-storm simulations, the no-storm results were subtracted from the dust storm results to construct the instantaneous forcing of the meteorological fields due to the dust loading. The column dust opacity of one case is mapped in Fig. 10, which depicts the evolving dust storm as it crosses over the proposed Mawrth Vallis landing site.

4.4.3 MRAMS Dusty Simulations

Recent improvements to the handling of dust within MRAMS are described in Rafkin (2011). In short, two distinct dust fields may be carried in the model. The first is a background dust field that may change in a user-specified way in space and time. The second is a perturbation dust field that is subject to changes due to lifting (Michaels 2006), sedimentation, condensation (if active), and transport by wind and diffusion. The perturbation dust field is constructed from eight tracers, with each tracer representing dust particles within a specified range of mass. Therefore, the perturbation dust size distribution is free to evolve in space and time. Typically, the background dust field is used to provide a baseline dust profile sufficient to maintain an atmosphere close to what is observed. For this project, the background dust profile was set identical to the MGS-TES-derived profiles used in the MGCM. This practice maintains consistency between the MGCM and MRAMS codes. In the case of dust storm simulations, perturbation dust was allowed to be lifted from the surface on the 4th grid. By controlling the efficiency of this lifting, the resulting opacity could be varied. An efficiency value was set so that perturbation opacities of three or greater were achieved. Both the background and perturbation dust fields were radiatively active. Although the dust storm was initially confined to the 4th grid due to the restrictions on lifting, the actual locations of lifting, dust mixing ratio and opacity, and dynamical response were not controlled. The dust storm was free to evolve in a purely consistent way with the dynamics and radiation, including the potential for radiative-dynamic feedback (Rafkin 2009).

Figure 11 shows the near-surface atmospheric circulation at the Mawrth Vallis landing site under a dust storm scenario and under the more typical undisturbed atmospheric conditions. Local dust storms were found to exhibit a completely different dynamical and thermodynamic regime; they were not just more extreme versions of quiescent conditions, but were entirely different (Rafkin 2009, 2011). End members from both the dust storm simulations and the nominal simulations were used to produce atmospheric profiles for input into the trajectory modeling. Thus, the modeling efforts spanned both dynamical regimes plus what may be nonphysical dynamical regimes between.
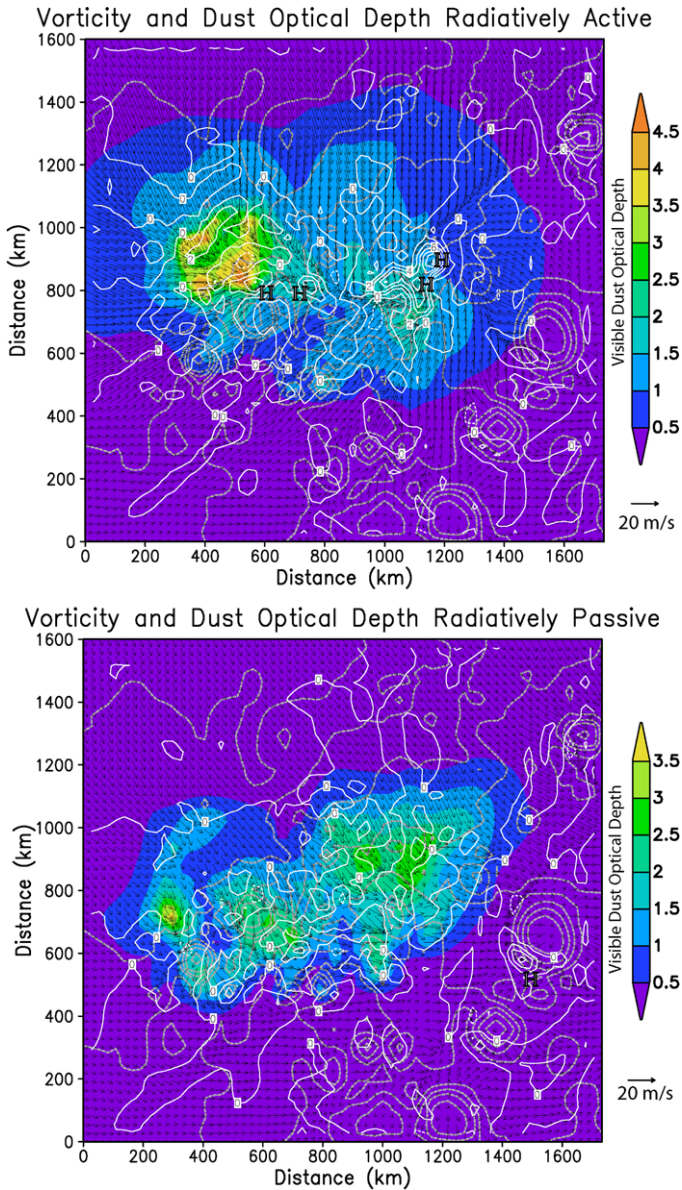
Fig. 11 Vorticity and optical depth in simulations where dust is radiatively active (*top*) or passive (*bottom*). Radiatively active dust substantially perturbs the dynamics compared to the passive case. In the former, winds speeds increase and strong circulations tend to develop near the most active dust lifting regions. The stronger winds tend to lift more dust, which produces a positive feedback mechanism. The *solid white contours* are vorticity ($\times 10^4$ s^{-1}), with maxima noted by "H". *Dashed lines* are topography. *Visible column* dust opacity is shaded. Wind vectors indicate magnitude and direction based on the reference 20 m s^{-1} vector below the *color bar*

4.5 Variability and Uncertainty

The ability to quantify uncertainty in the prediction of the atmospheric state for MSL EDL is limited by the coarseness of our knowledge and observations of Mars' atmosphere, as well as the inherent chaotic nature of their dynamics. Several approaches are used to establish the level of uncertainty. One is to use an ensemble modeling approach, where the differences between the results of independently developed numerical models are taken as a measure of uncertainty. This will capture uncertainty due to inherent and independent errors in the models, and to the extent that the models reproduce the natural variability, it will also capture the uncertainty due to the dynamics. Our two mesoscale models and the assimilated MGCM each produce a range of plausible states of the EDL conditions. The uncertainty in the prediction is taken as the union of the variability in both mesoscale models. Another key strategy is to use the variability within the models during the hours and days near the EDL event as a measure of the uncertainty at the time of the event. Further, all of the models have undergone extensive comparison with and validation against measurements, primarily vertical temperature profiles and surface pressure records. The above approaches address model numerical errors, systematic bias in the models relative to observations, and uncertainty due to true variability in the atmosphere from weather and thermal tides.

An important point must be emphasized with respect to MGCM initial conditions and the overall validity of predictions by the MGCM and mesoscale models. The predictions should not in any way be considered true forecasts of the precise conditions to be expected. In any planetary atmosphere, chaos will degrade the accuracy of any prediction over time even if the initial conditions are exact. In the case of Mars, the initial conditions are supplied only by climate models rather than observations, and the simulations are conducted years in advance of EDL. There is no possibility for a true prediction. Using an initial condition that matches the observations as closely as possible might be expected to produce the most probable climatological environment. But, the probability distribution of resulting circulations may actually be quite broad. Observations as far back as Viking show that the Mars atmosphere is not exactly repeatable from year to year; it is impossible to specify a singularly correct initial condition from which to begin a forecast. Further, the atmospheric circulation is strongly driven by the temperature distribution and the latitudinal and vertical thermal gradients in particular. Small changes in the thermal distribution such as might be achieved with reasonable dust profile perturbations can produce dramatically different mean and wave circulation patterns. A modestly different circulation pattern resulting from nearly the same thermal distribution may be almost as likely as the most probable circulation. Even if the models capture the average mean and wave patterns, it does not mean that the models will predict the phase and magnitude of a particular wave or storm system at a specific place or time. Whatever uncertainties are associated strictly with the mesoscale models must be added to the inherent uncertainties in the MGCM results. The uncertainty in the MGCM results from errors in physics and computation as well as errors resulting from the deviation of the model-produced climate from the actual atmospheric state at a given time. For all these reasons, the success of MSL EDL does not rely on a true forecast of the conditions upon arrival, but is designed and tested to be robust to a range of plausible atmospheric states, as described in the next section.

5 Assessment of EDL Atmospheric Safety

Because end-to-end flight tests in realistic Mars conditions are impossible, characterization of EDL system performance and safety margins is heavily dependent on end-to-end numerical simulations. Typically these are Monte Carlo simulations of the spacecraft from entry

through touchdown, utilizing detailed models of the vehicle, such as spacecraft shape, mass, and thrusters, and models of the environmental interaction, such as aerodynamics, terrain, and radar interaction with the terrain. Predictions of plausible atmospheric conditions are key inputs to these simulations.

Previous missions constructed atmospheric predictions for the entire trajectory based on vertical profiles of atmospheric parameters measured over the landing site. The advantage of this approach is that orbital instruments primarily return vertical profiles. The ∼100-km horizontal component of MSL's trajectory, however, may sample atmospheric variability that would not be captured in a process that defines the atmosphere over a single location. MSL could use multiple profiles, but the temporal and spatial coverage of measured profiles is not dense enough to capture a complete and physically consistent understanding of conditions along the trajectory. The mesoscale models discussed in Sect. 4, on the other hand, contain high-resolution fields of atmospheric parameters, tied together by the appropriate physical equations and boundary conditions. We sample these models in latitude, longitude, altitude, and time, as appropriate to capture conditions along the trajectory at the time of EDL (and also around that time in order to assess variability). Both mesoscale modeling groups delivered model output that spans at least 10 sols around the expected entry date, for each finalist landing site.

The MGCM that provides the fields to initialize the MRAMS mesoscale model was not tuned to precisely match VL pressures. While the seasonal amplitude excursions generally matched the VL data, there was a bias in that MGCM resulting from an inaccurately specified total CO_2 mass inventory. The bias was removed by scaling the pressures (and densities) downward by 3.9 % to match the Viking data as assimilated in the UKMGCM model (Sect. 4.1.2). The MMM5 pressures were within 1 % of the UKMGCM model and were not adjusted.

5.1 Representing Modeled Atmospheres in EDL Simulations

Integrating this huge volume (∼1 TByte) of mesoscale model data into the thousands of Monte Carlo simulations presented a computational challenge. To avoid handling the complete model output in each simulation, the team developed a methodology that utilizes the machinery within Mars-GRAM to statistically represent mesoscale model output in the EDL performance simulations. Mars-GRAM is a database of MGCM results and other atmospheric data. It also contains algorithms to extract profiles and statistically perturb them to create Monte Carlo distributions. The team used perturbed MGCM model profiles from Mars-GRAM for their early performance simulations. Because of this past experience and understanding of Mars-GRAM, the team decided to continue its use where appropriate, but to ultimately use the higher-resolution mesoscale models as the source of atmospheric data. By tuning the Mars-GRAM perturbation schemes, the desired characteristics of variability can be added to mean mesoscale profiles in order to create a dispersed set for Monte Carlo simulations (Cianciolo et al. 2008b).

5.1.1 Mars-GRAM

Mars-GRAM is an engineering-oriented atmospheric model used for a number of Mars mission applications, including systems design, performance analysis, and operations planning for aerobraking, EDL, and aerocapture (Justus et al. 2002). Mars-GRAM outputs include density, temperature, pressure, winds, and selected atmospheric constituents. Mars-GRAM has been validated against radio occultation data, and both nadir and limb profiles from MGS-TES (Justus et al. 2004, 2005).

There are several options in Mars-GRAM for representing the unperturbed atmosphere along the EDL corridor. The first option is for the user to specify the atmospheric dust (e.g., optical depth, vertical distribution, and particle characteristics). The remaining atmospheric data are interpolated from NASA Ames MGCM (Haberle et al. 1993a) model runs conducted using a range of globally uniform dust optical depths. The second option is to draw the atmospheric data from user-input auxiliary profiles of temperature and density versus altitude. Examples of auxiliary profiles include MGS-TES (nadir or limb) observations, or Mars mesoscale models output at a particular location and time. Another option is to use dust optical depths as measured spatially and temporally in one of the MGS-TES mapping years, with the remaining data interpolated from the NASA MGCM runs.

Mars-GRAM can also output profiles that include perturbations from the mean. This capability has been used in a Monte Carlo mode to perform high-fidelity engineering end-to-end simulations for EDL. Three Mars-GRAM parameters control the standard deviations of the perturbations: *rpscale* can be used to scale the magnitude of density perturbations; *rwscale* can be used to scale the magnitude of wind perturbations; and *wlscale* can be used to adjust the wavelengths (spectral range) of the perturbations. As described below, we use Mars-GRAM primarily to apply perturbations to profiles supplied from our mesoscale models.

5.1.2 Creating Lookup Tables from the Mesoscale Models and Mars-GRAM

First, an approximate entry trajectory used to query the mesoscale models is found using the predicted arrival azimuth (relative to the target) and the approximate range from atmosphere entry to parachute deploy. At Gale, azimuth at the target varies through the launch window from 91° to 101° (clockwise from north), and range is ∼700 km. Trajectories for each day of the launch window are plotted in Fig. 12. The trajectory at the middle of the azimuth range was selected for the mesoscale model query. Vertical profiles then are sampled from the mesoscale output along this trajectory and at model time steps between 1200 and 1700 hr on all available sols. Because the vehicle slows as it approaches the landing site, the spatial density of sampling increases nearer to the site in order to better represent the variability within the mesoscale models. At distances >400 km from the target, profiles are 25 km apart, between 400 and 140 km, profiles are 10 km apart. From 140 to 10 km distance, the spacing decreases to 4 km. Within 10 km of the landing site, sampling is done every 1 km. This sampling scheme is depicted in Fig. 13. Vertical sampling occurs every 10 m from the surface to 1 km, every 100 m from 1 km to 10 km above the surface, and every 500 m for altitudes above 10 km.

Given the lack of measurements sufficient to quantify the uncertainty in winds and density, we use the variability within the MRAMS and MMM5 mesoscale models in the hours and days near the entry time as a proxy for uncertainty. For each vertical profile extracted from the models, the mean and standard deviation of the temperature, pressure, density, and wind (in three dimensions) are calculated using a 5-hr window around the expected entry time and at least 10 sols around the expected entry date. These standard deviations were used to choose the Mars-GRAM *rpscale* and *rwscale* perturbation factors. In this way, Mars-GRAM statistically captures the mesoscale data and can pass that information on to the performance simulations. As a check, the statistically generated profiles are compared with raw model profiles, as illustrated in Fig. 14.

A set of dispersed profiles can be made for each mesoscale model, or jointly in order to capture the combined total variability of each parameter. To generate combination atmosphere lookup tables, the means of both model outputs are averaged and a perturbation
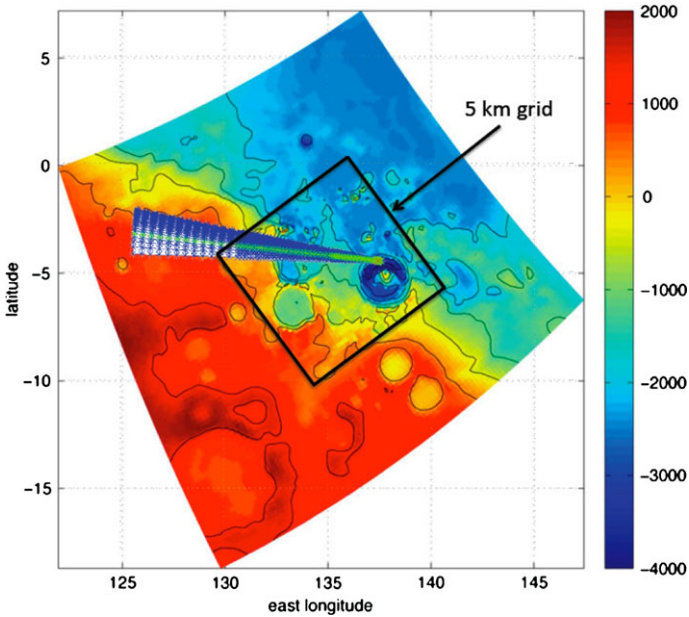
Fig. 12 Possible trajectories at Gale crater over the range of launch dates, plotted on a topographic map, in meters. The *bottom line* denotes the open of the launch window and the *top curve* denotes the close of the launch window. The *green line* at day 5 in the launch window is near the middle of the azimuth range and was selected for the mesoscale model query. MSL launched on day 2, with a predicted arrival azimuth of 93°
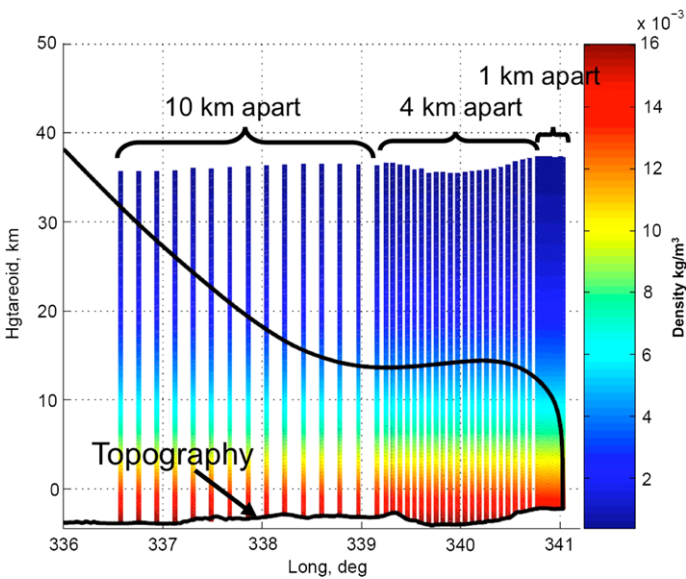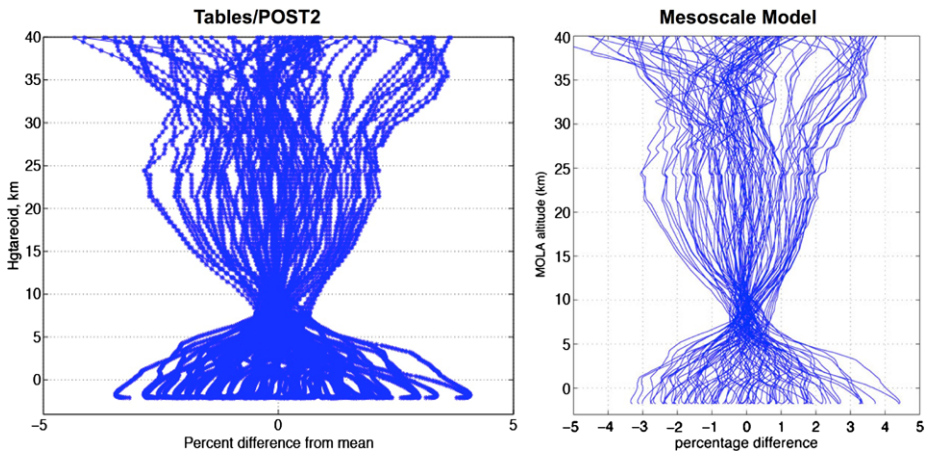

Fig. 13 Scheme for sampling mesoscale atmospheric models

Fig. 14 Comparison of density profiles generated by statistically sampling the mesoscale model output with those directly extracted. This example is for the MMM5 model and Holden crater landing site

envelope around the combined mean is constructed by capturing the larger of each model's variability at every altitude. Requiring that the EDL system show adequate performance margin against this combined range of potential atmospheric conditions forces the system to be more robust. This approach is especially useful at Gale crater, where the zonal winds and density calculated by the two mesoscale models diverge significantly (Figs. 15 and 16). Given the better agreement at the other finalist sites, we attribute the differences at Gale crater to its equatorial latitude. Equatorial dynamics are challenging to model due to the relative unimportance of the Coriolis force, which then allows a variety of other more variable and highly parameterized processes (e.g., advection, diffusion, turbulent mixing, radiative forcing, dust loading, and thermal tides) to determine net accelerations.

5.2 Adding Wind and Density Perturbations Beyond Modeled Ranges

At this stage, we have the option to additionally inflate the magnitude of density and wind perturbations over the mesoscale model values, in order to include sources of uncertainty not captured by the models, or to assess performance against more difficult atmospheric conditions. After tables are created from the mesoscale data, an additional density perturbation of ±10 % (uniform distribution) is applied. This distribution is intended to represent the uncertainty in Mars' surface pressure at the landing site, which is expected to be ±5–6 % (3-sigma), along with added safety margin (Withers 2012).

To add safety margin to the mesoscale wind statistics, the EDL team calculates the 3-sigma variability of the steady-state winds in the model data and uses those bounds to perturb steady state winds in the simulations. Then another 3-sigma magnitude high-frequency perturbation is added on top of the steady state component. In addition to perturbation wind magnitudes, the length scale or spatial frequency can also be varied to stress EDL system performance. An example for the Mawrth Vallis candidate landing site (Fig. 17) shows several sample profiles where steady state wind and high-frequency wind perturbations have been applied using model output as the basis for the wind directions and magnitudes.
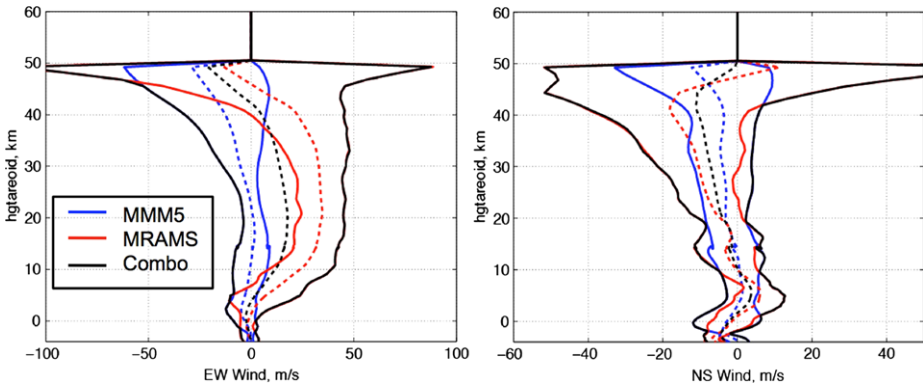
Fig. 15 Variability of east-west (*left*) and north-south (*right*) winds in the mesoscale models. *Dashed lines* are the means of each model and of the combined output. *Solid lines* show the 3-sigma bounds of each model and the combined envelope used in the simulations

Fig. 16 Variability of density in the mesoscale models. *Solid lines* show the 3-sigma bounds within each model and the combined envelope used in the simulations. Variability is shown relative to the mean of the combined model output
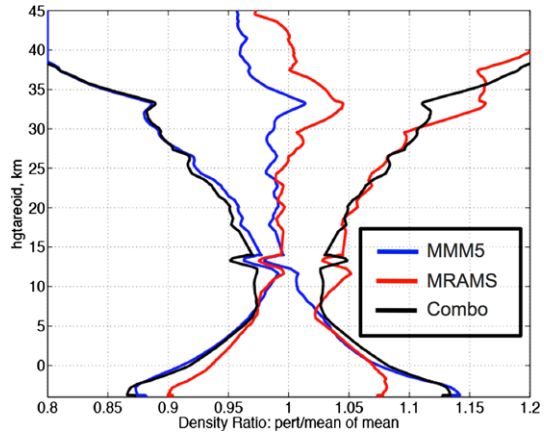
5.3 Case-Consistent Model Extractions

The approach we have described captures the statistical variability present in the model atmospheres, but ultimately creates synthetic profiles for the simulations. While this approach is useful for testing and stressing the EDL performance, it may destroy coherent atmospheric structures, such as waves generated at particular scales or updrafts locked to surface terrain. In order to assess performance of the highly nonlinear EDL control algorithms against these types of atmospheric structures, we have developed a case-consistent modeling approach. This method selects a snapshot of data from the model at a particular sol and local time. It then extracts vertical profiles along the nominal trajectory and at nearby points (Fig. 18). These values are fed directly into the simulation, without adding perturbations. As the vehicle's simulated flight moves away from the initial trajectory guess, the other profiles are introduced, ensuring that the vehicle encounters any coherent atmosphere structures. While an important part of our overall safety assessment, the simulations show no special sensitivity to such structures. As a result, these runs are much less stressing than our runs that attempt to capture the full (or even further enhanced) variability present in the models.

Fig. 17 Perturbed meridional wind profiles for the Mawrth Vallis landing site. *Solid red lines* denote the bounds of the steady state wind. The *dashed red lines* denote the maximum value that the high-frequency wind can generate around a steady state profile. *Blue lines* illustrate ten individual Monte Carlo trajectories
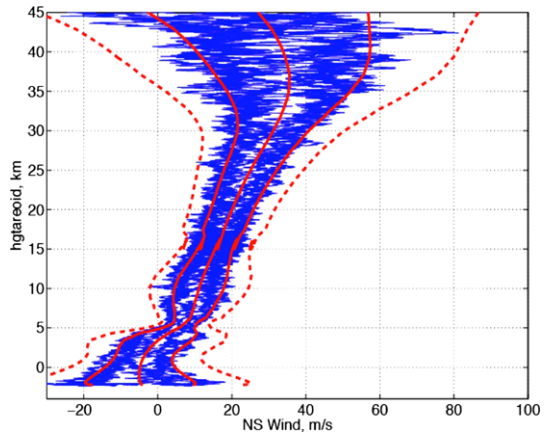
Fig. 18 Three-dimensional scheme for sampling particular mesoscale model cases along the entry corridor. *Black lines* correspond to the minimum and maximum latitude range as a function of longitude for a 2000-case Monte Carlo analysis of the MSL entry. The *colored dots* represent locations of mesoscale vertical profiles approximately 4 km apart. The *different colors* show the 4-km latitudinal spacing of the sampling
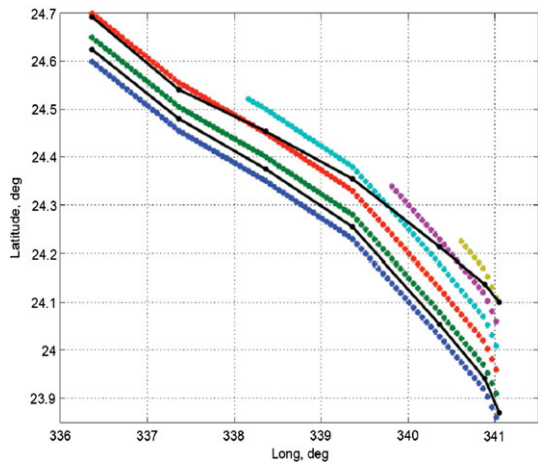
5.4 Performance Results for the Finalist Sites

Having constructed a set of Monte Carlo and case-consistent simulations, the EDL performance could be interrogated. The analysis looked at the entire trajectory for each of several thousand runs, noting key performance parameters such as parachute deploy conditions, propellant usage, and touchdown footprint statistics. Prior to the MSL landing site selection in July 2011, the team presented EDL performance and margin results for the final four candidate landing sites at a Landing Site Safety Assessment Review. The team and review board concluded that the risk to the spacecraft during atmospheric flight was acceptably low at all of the sites, and furthermore, that the distinctions in risk level between the sites should not play a role in discriminating between sites. The site selection process is fully described by Golombek et al. (2012).

The results for Gale crater contain adequate EDL margins in areas of concern such as parachute deploy conditions (e.g., Mach number and dynamic pressure) and landing uncertainty ellipse size (Fig. 19). Other key margins, such as timeline and fuel, also are robust. Less than 1 % of the Gale crater Monte Carlo cases encounter conditions that are considered
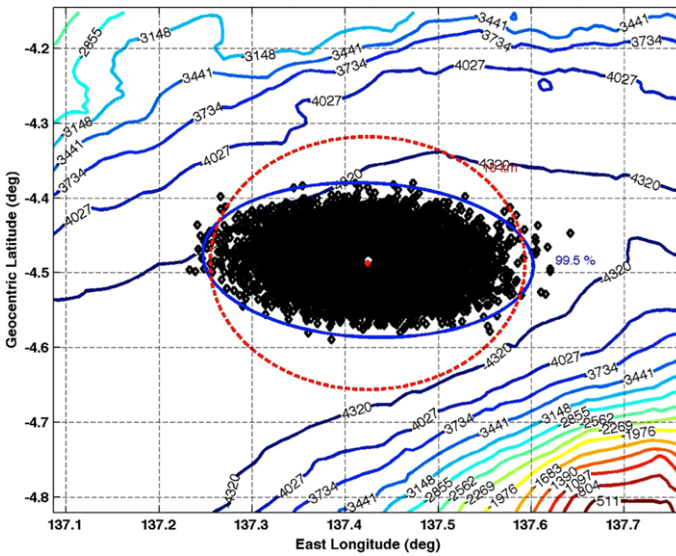
Fig. 19 Distribution of landing points for EDL simulations using the combined model atmospheres. The *blue ellipse* is the 3-sigma envelope. The *red circle* (showing as an ellipse in this map projection), defines the required ability to land within 12.5 km of the target point. The *colored contours* show MOLA elevation with labels in meters

out of specification. Only a small subset of those are mission-ending, most due to encountering unsafe terrain upon landing (within the nominal landing error ellipse).

5.5 Assessing Performance Against Atypical Dust Events

Due to the possibility of regional dust events at our landing sites, an effort has been made to model their effects and investigate the impact on EDL performance. Using orbiter observations of past dust events in our landing season, mesoscale models have been tuned to attempt to capture the impact of the dust events on atmosphere characteristics of interest, such as density and winds. Results from these mesoscale dust cases (Sect. 4.4) have been used to generate atmosphere tables, just as with the nominal mesoscale results. EDL performance simulations utilize these tables to quantify the EDL performance impact of dusty atmospheres. The EDL system's robustness is evident in its performance against the dusty atmospheres. Performance changes relative to the nominal atmospheres are slight: landing uncertainty is almost identical and other margins are only weakly affected. The risk associated with regional dust events is judged to be acceptably small.

5.6 Remaining Pre-EDL Assessment Activities

As with past Mars lander missions, the team will monitor atmospheric conditions near the landing region as the vehicle approaches Mars, using MRO-MCS profiles and MRO-MARCI imagery. The Council of Atmospheres will meet with increasing frequency in the weeks before entry, with daily meetings during the final week. Under most circumstances, EDL will be executed as planned, with parameters that allow a safe flight through the range of expected conditions. However, if the orbital monitoring indicates a large and persistent disturbance over the landing region in the days before entry, the team may choose to simulate the EDL

performance through the inferred conditions and adjust EDL parameters to increase the margin of safety.

6 Thermal Environments for Surface Operations

Early in the project's history, a set of thermal environmental requirements was defined to guide the design and testing of the rover for its surface operations phase on Mars. These requirements include ground and near-surface air temperatures, wind speeds, and atmospheric dust opacity and fallout rates. Ground and air temperatures, and their coupled effects with wind speed via advective heat transfer, have the greatest impact on the MSL rover design. In cold conditions, the rover draws heat from its radioisotope thermoelectric generator and delivers that heat to the rover electronics and instruments using a fluid loop. In warm conditions, the fluid transfers heat from the rover interior to radiators, where it is rejected to the environment. This subsystem is designed to keep a thermal interface to internally mounted electronics within a $\sim$90 °C temperature range despite the potential for a $\sim$160 °C range of diurnal and seasonal ground temperatures (and the additional heat generated by the electronics themselves).

Further, elements that are not in contact with the fluid loop, such as externally mounted instruments and actuators, can require a significant portion of the rover's daily energy budget to reach operating temperatures using electrical heaters. Accurate engineering simulations are needed to calculate energy estimates each day of the mission for use in the science operations planning process. Without solar panels, MSL is much less affected by atmospheric dust opacity or deposition than previous landers or rovers. But atmospheric dust changes the direct and diffuse insolation, and changes the downward IR flux that controls the efficiency of heat radiation at night. Dust deposition on the rover will change the albedo and emissivity of its surfaces, and must be taken into account in the design. The ability of the total rover system (e.g., electrical and thermal power supplies, fluid loop, electrical heaters, rover absorptive and radiative properties) to meet the goals of the mission was assessed using the environmental requirements discussed below.

Ground and air temperatures are dependent on the landing site, primarily through latitude, but also through the site's albedo, thermal inertia (and IR emissivity, though this quantity varies little around Mars), and meteorological activity. Initially, landing sites up to $\pm$60° latitude were considered. The lower limit on ground and air temperature on Mars is set by the condensation point of CO_2, the primary atmospheric constituent ($\sim$−130 °C). At sites near 60° latitude in winter, the rover would encounter temperatures fixed at the CO_2 frost point for months at a time, resulting in reduced performance if not total hibernation. After an initial survey of candidate sites showed few compelling destinations poleward of $\pm$30°, NASA chose to reduce the site selection to $\pm$45°, then finally to $\pm$30°, primarily to avoid very cold winter conditions.

Transient periods of CO_2 frost temperatures cannot be ruled out even for some of the higher-latitude finalist sites (Table 1), but the mission can accept limited productivity at those times without significantly affecting mission goals. The final MSL thermal design views CO_2 frost temperature as a constraint on survival; the rover is designed to survive indefinitely at those temperatures (along with a cold wind and clear atmospheric conditions). However, a much greater fraction of the total available energy will be required to warm actuators and other hardware in those conditions, reducing productivity.

6.1 Inputs to Surface Thermal Environment Assessments

As with the EDL cases discussed earlier, to provide the needed bounds for engineering simulations, we took the approach of commissioning runs from scientific models that are constrained by and validated against the best available measurements from Mars. With models, we can create continuous temporal profiles of ground and air temperature, in spite of the sparse coverage of measurements. One-dimensional surface-atmosphere models are sufficient for estimating ground and near-surface air temperature (though dynamical effects are not captured), given reasonably accurate inputs of atmospheric dust opacity, and surface thermal inertia and albedo. We used two independent models to allow cross-validation. Ground temperatures insolation are taken from a 1-D model run at JPL, while air temperatures are taken from a 1-D version of the Ames MGCM run at NMSU. There is very good general agreement between the models (see Sect. 6.3). The JPL model has more accurate ground temperatures because it runs continuously over the year and captures seasonal effects. The Ames model, while run only for snapshots of L_s, is better validated for near-surface air temperature calculations.

6.1.1 JPL 1-D Surface-Atmosphere Model

The JPL 1-D model is an efficient, coupled surface-atmospheric model with radiative transfer and sensible heating physics based on the GFDL MGCM circa 2004 (Hinson and Wilson 2004). The model contains standard routines for calculating insolation, subsurface heat conduction, atmospheric convective adjustment, and CO_2 pressure and frost evolution. Because the model in the form used here does not appear in the literature, we include a detailed description here. Model parameters are listed in Tables 3 and 4.

Model surface temperature is determined by the instantaneous balance of fluxes due to insolation, IR radiation from atmospheric CO_2 and dust, sensible heat exchange, subsurface conduction, and surface thermal emission. The subsurface is divided into thirty layers that extend deep enough to capture the attenuation of diurnal and seasonal temperature variations. Conduction between layers is computed using an explicit scheme, so layer thicknesses are set by a numerical stability criterion once the model time step is chosen. Each layer can have a unique thermal conductivity, heat capacity and density. In practice, for all layers the density is fixed and the heat capacity varies with temperature (Ledlow et al. 1992). The thermal conductivity is calculated from the input thermal inertia (a free parameter), the density, and a heat capacity appropriate for the mean annual surface temperature at that point.

The atmosphere is divided into 20 layers extending from the surface to ∼70 km. Atmospheric CO_2 and dust modify atmospheric and surface temperatures through absorption, scattering, and emission. Heating through absorption of sunlight in the near-IR bands of atmospheric CO_2 is calculated as described by Forget et al. (1999). Computational efficiency necessitate Planck-weighted, spectral averages of the dust single scattering albedo, ω, phase function asymmetry parameter, g, and extinction cross-section, C_{ext}. Accordingly, radiative transfer calculations are performed within one solar and three IR bands. The interaction of sunlight with dust is modeled over the 0.1–5 μm wavelength region. Solar-band extinction and heating rates for dust are found using the two-stream delta-Eddington approximation for aerosol scattering (Joseph et al. 1976; Briegleb 1992). We chose solar-band dust properties (Table 4) that are consistent with a suite of orbital and lander-based studies (Clancy et al. 2003; Tomaksso et al. 1999; Pollack et al. 1995).

The treatment of IR radiation closely follows those of Forget et al. (1999) and Hinson and Wilson (2004). IR radiation is separated into three wavelength regions, 5–11.6 μm,

Table 3 Parameters used in the JPL 1-D thermal model

Parameter	Value
Regolith density	$1500 \, \mathrm{kg \, m^{-3}}$
Planetary heat flux	$0 \, \mathrm{W \, m^{-2}}$
Regolith emissivity	0.98
CO_2 frost albedo	0.6
CO_2 frost emissivity	0.8
CO_2 frost latent heat	$5.9 \times 10^5 \, \mathrm{J \, kg^{-1}}$
Dust effective radius	$1.5 \, \mathrm{\mu m}$
Dust radius variance	$0.4 \, \mathrm{\mu m}$
Boundary layer wind speed	$10 \, \mathrm{m \, s^{-1}}$
Surface roughness length	0.01 m

Table 4 Dust radiative parameters used in the JPL 1-D thermal model

Wavelength region	Single-scattering albedo	Asymmetry parameter	Normalized extinction cross-section	Normalized absorption cross-section
0.1–5.0 μm (solar)	0.92	0.65	1.0	–
5–11.6 μm (IR)	0.3326	0.5033	0.3840	–
11.6–20 μm (IR)	0.1871	0.3736	0.2296	0.1866
20–100 μm (IR)	0.1050	0.1796	0.1913	–

11.6–20 μm, and 20–100 μm, in order to isolate the broad CO_2 absorption band near 15 μm. Within the 11.6–20-μm band, scattering is ignored and dust is treated as a grey absorber. The absorption cross-section $C_{abs} \equiv (1 - \omega)C_{ext}$. Absorption and emission by CO_2 near the 15-μm band are calculated using the numerical approximation of Hourdin (1992). In the remaining two IR regions, a two-stream algorithm is used that includes multiple scattering for dust (Toon et al. 1989). Dust IR properties correspond to a "palagonite-like" composition and a modified gamma size distribution with an effective (cross-section weighted) radius of 1.5 μm and a radius variance of 0.4 μm, computed at a temperature of 215 K (Wolff and Clancy 2003). The results from spectrally resolved calculations (Michael Wolff, personal communication) have been averaged over our modeled wavelength regions. The IR extinction efficiencies listed in Table 4 are normalized to the solar band and result in a visible-to-IR opacity ratio of ∼1.67 (at an IR wavelength of 9 μm).

Column dust opacity, a free parameter, is used to scale a time-invariant, spatially uniform dust distribution. Dust mixing ratio is relatively constant with height in the lower atmosphere, but falls off above ∼35 km (Conrath 1975). After heating rates are applied to the atmospheric column, a convective adjustment algorithm redistributes excess entropy. The radiative effects of water ice are not modeled. Sensible heat exchange between the surface and atmosphere is modeled using a Monin-Obukhov boundary layer scheme developed for terrestrial models (Hicks 1976). Wind speed is assumed to be constant. We use a globally uniform surface roughness length that is representative of the Viking Lander sites and terrestrial deserts (Sutton et al. 1978).

Model atmospheric pressure varies seasonally according to VL-1 measurements as fit by Hourdin et al. (1995). The surface pressure is scaled to the modeled location using MGS-MOLA topography and a scale height of 9.25 km. Condensation of CO_2 at the modeled

location is calculated separately. If the model surface temperature falls below the frost point temperature, it is fixed at the frost point and the surface albedo and emissivity are modified. At subsequent time steps, the surface energy balance determines whether CO_2 condenses or sublimates until the CO_2 is depleted. The frost point is parameterized as $T_{\text{frost}} = 149.16 + 6.476 \ln(0.13499 P)$, where T is in Kelvin and P is the surface pressure in millibars (Mellon et al. 2000).

A novel feature of our model is its integration with the JPL Navigation and Ancillary Information Facility (NAIF) Toolkit (Acton 1996). NAIF routines and kernels calculate temporal and geometric quantities for planetary bodies and spacecraft. We use them to find solar distance and incidence angle as functions of ephemeris time, latitude, and longitude on Mars. By doing so, our model runs are very precisely linked to the data that we wish to simulate. Mars L_s is found using the expressions of Allison (2000). We use a model time step of 1/96 of a Martian day. Initial conditions are removed by running the model for four model years and re-initializing the subsurface to computed average surface temperatures after the second year.

Results from the JPL model compare well with other 1-D coupled models (e.g., Paige et al. 1994; Mellon et al. 2000), although some differences are expected due to the incorporation of physical algorithms and parameters (e.g., dust optical properties) that reflect a more recent state of knowledge, the use of a different CO_2 radiation scheme, and the inclusion of forced (wind-driven) convection at night. Small differences also are expected due to the other novel features of the JPL model, such as temperature-dependent heat capacity and incorporation of the annual pressure cycle.

6.1.2 NMSU 1-D MGCM

The NMSU model generates ground and near-surface air temperatures with a 1-D radiative-convective version of the NASA Ames MGCM (Pollack et al. 1990; Haberle et al. 1997, 1999; Martin et al. 2003; Tsuyuki et al. 2007). This model has previously been successfully employed to provide predictive and operational environmental conditions for MER (Martin et al. 2003) and the Mars Phoenix Lander (Tamppari et al. 2008; Tsuyuki et al. 2007).

The model determines atmospheric heating and cooling by accounting for absorption of solar (visible and near-IR) radiation by both CO_2 gas and suspended dust, and the absorption and emission of IR radiation (within two bands, the 15 μm band and all others) by dust and CO_2. Condensate cloud and water vapor are not accounted for. Seasonally, daily, and latitudinally dependent variation of downward solar flux is accounted for. The surface is warmed or cooled by the net radiative flux divergence at the atmosphere-surface interface as well as sensible heat exchange with the atmosphere in contact with the surface. Vertical atmospheric mixing is included, with its intensity dependent upon local Richardson number stability criteria (Haberle et al. 1993b, 1999). Surface roughness is specified to be 1 cm. In this 1-D configuration, near-surface horizontal winds are set to a nominally small (3 m s^{-1}) value for turbulence calculation purposes. The model also includes a 12-layer soil model to determine diffusion of heat into and out of the upper 0.25 m of the regolith. This depth accounts for the penetration of the diurnal thermal wave, but is shallower than the depth of the seasonal thermal wave.

Model results include ground temperature, near-surface air temperatures from 1.5 to 20 m altitudes, ground-level downward solar flux and downward IR, all of which are generated at a specific latitude-longitude location. These temperatures and downward flux values at the surface are dependent upon latitude, L_s, surface pressure (dependent upon topography and season), thermal inertia, albedo, and dust optical depth. Atmospheric dust has a specified
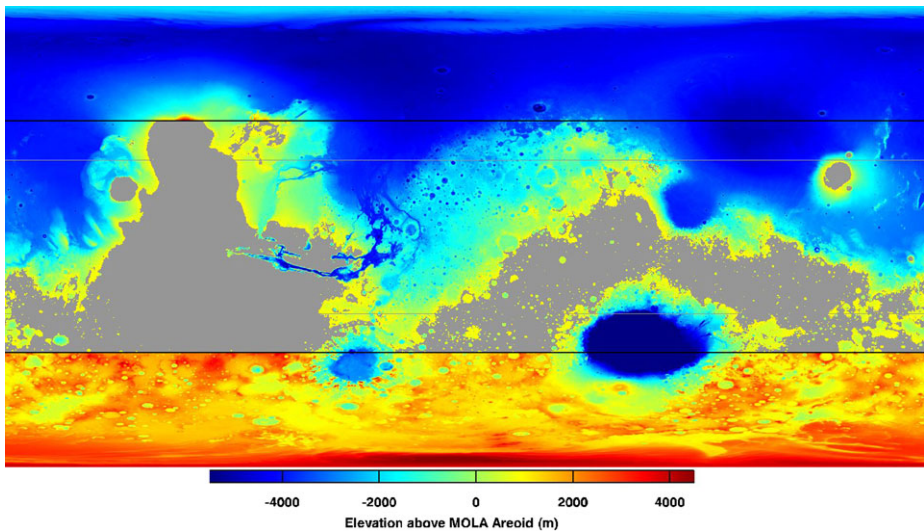
Fig. 20 Mars surface elevation as determined from MGS-MOLA, referenced to the MOLA areoid. Regions above 1 km elevation are greyed out (not above ±45° for clarity). *Lines* are drawn at ±45° latitude indicating the bounds of the region considered in the Worst Case thermal studies. The map shows −180° to 180° east longitude and ±90° latitude

visible-to-infrared opacity ratio value of 2.0 and prescribed vertical profile of mixing ratio (Conrath 1975). Model simulations span 50 sols from an initial prescribed isothermal state. Model time step is ∼500 seconds, which results in 160 time steps per simulated sol. Seasonal date remains constant during the simulation. Model convergence (sol-to-sol temperature variations less than 0.1 K) is well achieved within this 50 sol time period.

6.1.3 Measurements of Albedo, Thermal Inertia, and Atmospheric Dust Opacity

Maps of surface elevation, albedo, and thermal inertia are shown in Figs. 20, 21, 22. Elevation and albedo are from the Planetary Data System. Thermal inertia maps are 2007-era maps produced by Nathaniel Putzig (personal communication). Atmospheric dust opacities are taken from MGS-TES, which measures the column opacity at 9-μm. Visible-wavelength opacities are estimated to be between 1 and 2 times the 9-μm values, depending on the model used.

6.2 MSL Worst Case Studies for Sites ±45° Latitude

To assess rover survival and operability over potential landing sites within ±45° latitude (and the mission requirement of <1 km elevation), we needed to understand the range of plausible ground and air temperatures at all relevant locations. Dust opacities vary significantly with latitude and season over the region relevant to MSL. Based on an inspection of MGS-TES data, we use a 9-μm value of 0.1 to denote clear conditions and a value of 0.75 for a very dusty atmosphere. (Regions of active dust lifting within storms can have much higher opacities but are not considered here.) Four cases were of interest to the rover designers. First is a Daytime Hot Case, defined as the site and season where the effects of latitude, dust opacity, albedo, and thermal inertia result in the warmest daytime ground and
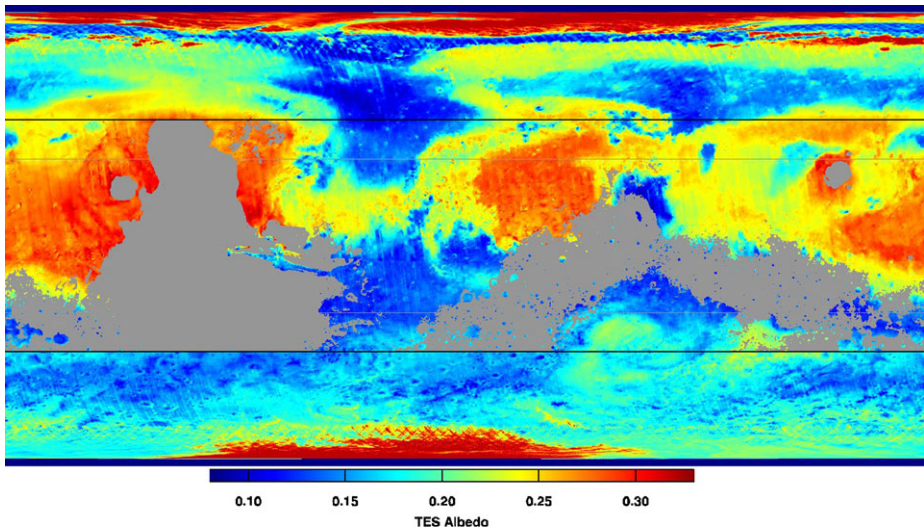
Fig. 21 Mars surface albedo as determined from MGS-TES
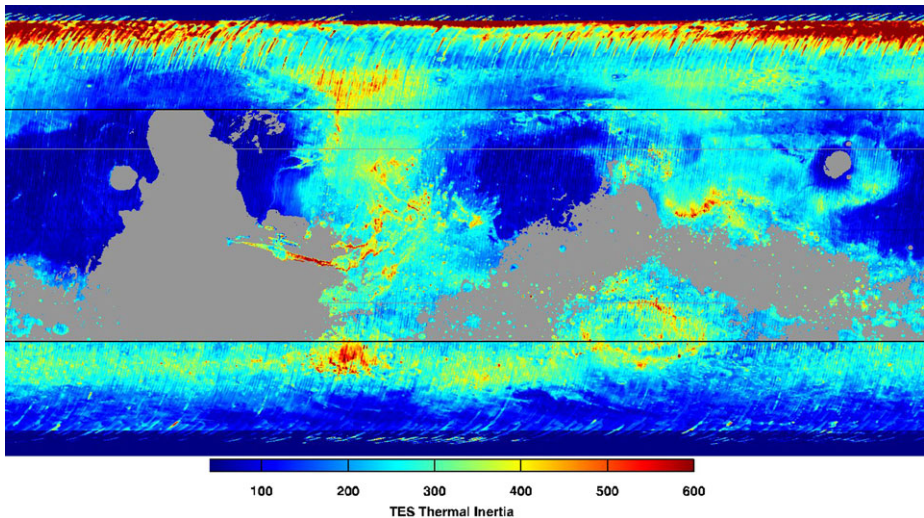
Fig. 22 Mars surface bulk thermal inertia as determined from MGS-TES

air temperatures. Next is a Nighttime Cold Case, where nighttime temperature is the lowest. Third is the Diurnal Range Case, where the largest amplitude diurnal temperature swing occurs (a factor relevant to part and packaging design). Finally a Nighttime Hot Case has the warmest nighttime temperatures (a factor that inhibits radiative cooling of the vehicle).

The results from the worst case studies are listed in Table 5. Because of Mars' eccentric orbit and argument of perihelion, southern mid-latitudes have more extreme seasonal variations than other relevant latitudes. These latitudes experience both a long, cold winter and a short, hot summer. Accordingly, the Daytime Hot Case is defined near the sub-solar latitude in southern summer (slightly offset in latitude due to the grid point locations of the

Table 5 Parameters used in worst case thermal studies

Worst case	Dust opacity (visible)	Albedo	L_s	Thermal inertia $(J\,m^{-2}\,K^{-1}\,s^{-1/2})$	Latitude	Ground temp. (°C)	1-m air temp. (°C)
Daytime hot	0.2	0.12	270.0°	220	−27.5°	38	13
Nighttime cold	0.2	0.22	90.0°	250	−45°	−127	−126
Diurnal range	0.2	0.28	270.0°	75	0°	−116 to 24 ($\Delta T = 140$)	N/A
Nighttime hot	1.5	0.15	270.0°	350	−40.0°	−59	−58

Table 6 Parameters used to model the finalist sites and the fictitious thermal design site. Thermal inertia is in SI units

Landing site	Albedo	Thermal inertia
Eberswalde	0.12	375
Gale Crater	0.25	350
Holden Crater	0.13	350
Mawrth Vallis	0.15	350
27.5°S Fictitious	0.12	220

MGCM), using values of albedo, thermal inertia, and dust opacity at the low end of their observed ranges in the ±45° region. The Nighttime Cold Case is set by the presence of CO_2 frost temperatures. Surfaces at higher latitudes in winter with higher albedos and thermal inertias, and lower dust opacities, are more likely to accumulate CO_2 frost. The Diurnal Range Case is defined at the equator, for a surface with a low thermal inertia and low dust opacity. Albedo and season are not significant factors. Finally, the Nighttime Hot Case is defined at a higher southern latitude site in summer with low albedo, high thermal inertia, and most importantly, high dust opacity. High dust opacity buffers surface temperature by lowering insolation during the day, warming the atmosphere, and preventing efficient radiative cooling of the ground at night.

6.3 Thermal Studies of the Finalist Landing Sites

When the finalist sites were selected in 2008 (Table 1), the rover thermal requirements were revised in order to provide the thermal engineering team with profiles relevant to the actual sites, rather than worst-case bounds. In addition to calculating profiles for each site, we also constructed a profile for a fictitious site at 27.5°S that bounded the range of temperatures at all four sites, with additional margin for uncertainty and error. The parameters for these sites are listed in Table 6. For a complete discussion of the site albedo, thermal inertia, and other characteristics, see Golombek et al. (2012). The values of albedo and thermal inertia used here differ slightly from Golombek's due to refinements they applied after our study and due to deliberate choices on our part to use thermal inertias that are slightly lower than measured site averages (resulting in a broader range of temperatures). For all of the candidate sites we used a variable atmospheric dust opacity, with the 9-μm opacity set to 0.1 from $L_s = 0°$ to 180°, and 0.35 from $L_s = 180°$ to 360°, with a ramp at each boundary. This scenario is based on an inspection of MGS-TES data near the sites. For the 27.5°S case, the opacity is fixed at 0.1.

Figure 23 shows profiles of ground temperature over the Martian year for the four finalist sites and the 27.5°S case. The higher-latitude, southern-hemisphere sites experience both

Fig. 23 Ground temperatures at the finalist sites and fictitious site at 27.5°S. The maximum (*upper set of lines*) and minimum (*lower set*) diurnal temperatures are plotted each sol (i.e., Mars day) starting at $L_s = 0°$. MSL arrives at $L_s = 151°$, or sol 318 on this plot. When plotted vs. sol, the asymmetric length of the seasons that arises from Mars' eccentricity is more apparent than on plots vs. L_s (cf., Fig. 25)
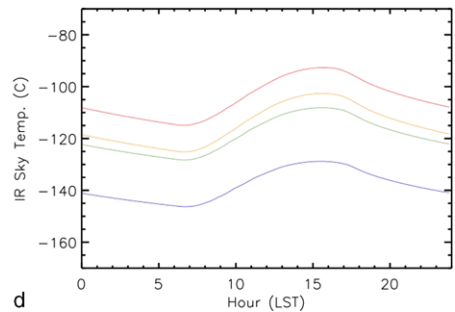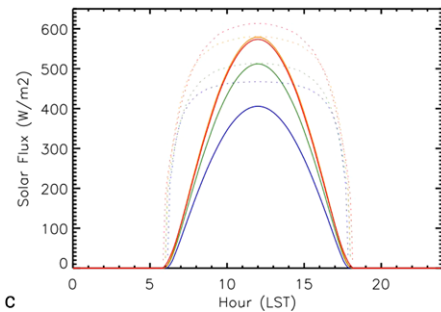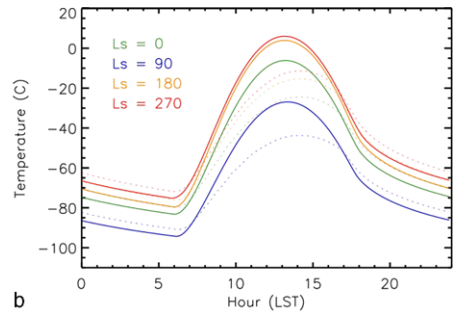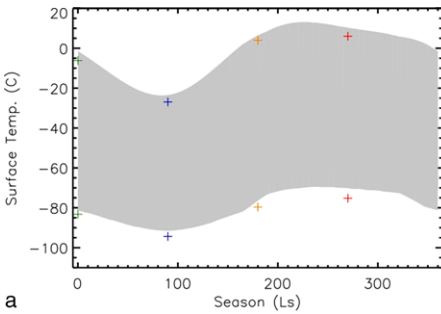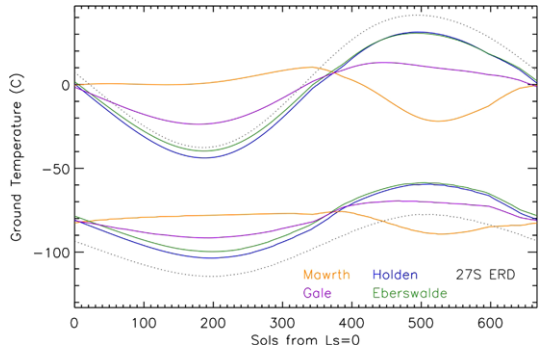

Fig. 24 Environmental results for the Gale crater landing site. (**a**) Surface temperature over the Martian year from the JPL model. The *grey area* shows diurnal temperature cycles at four seasons. The *colored symbols* are the output from the NMSU model at $L_s = 0°$, 90°, 180°, and 270°. (**b**) *Diurnal cycles* of ground temperature (*solid*) and 1-m air temperature (*dotted*), both from the NMSU model. (**c**) Diurnal cycles of normal (*solid*) and directional (*dotted*) solar flux from the JPL model. (**d**) Diurnal cycles of sky temperature from the JPL model

the coldest and warmest temperatures over the year, with longer winters than summers, as expected due to Mars' eccentricity and argument of perihelion. The Mawrth Vallis site is at a similar latitude but in the northern hemisphere, and therefore experiences more moderate seasons and a shorter winter. Gale crater, while nearly equatorial, exhibits a southern-hemisphere pattern of seasonality due to Mars' eccentricity. The seasons are moderate, but the winter is long. Figure 24 shows ground, 1-m air, and sky temperatures, and incident solar flux at the Gale crater landing site. Sky temperature is the downward IR flux converted to an equivalent blackbody temperature.
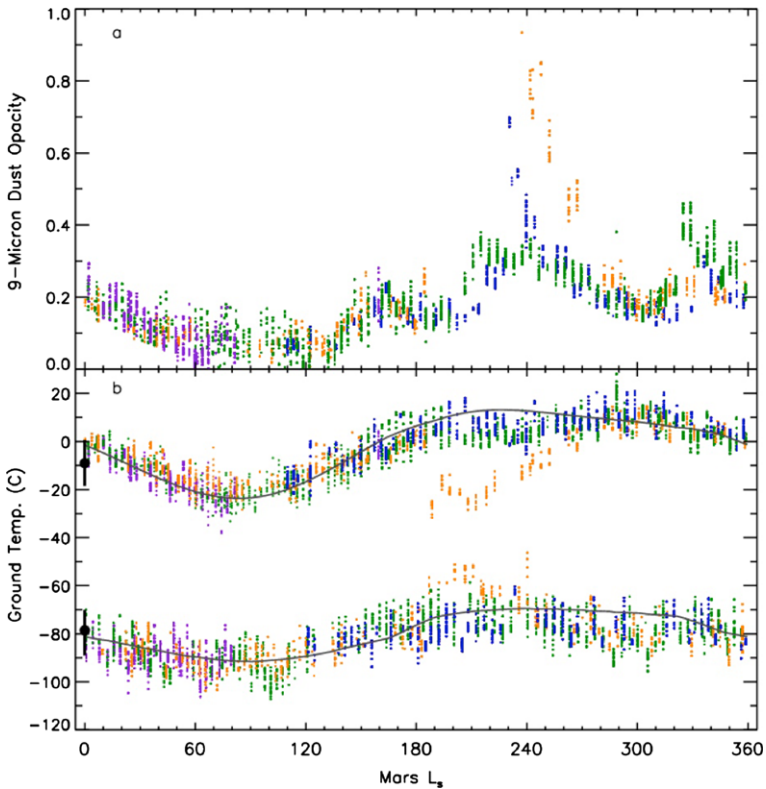
Fig. 25 Atmospheric dust opacity and ground temperature at Gale crater over more than three Mars years (mid MY24 to mid MY27). (**a**) MGS-TES measurements of 9-µm column opacity in a box 4° longitude by 2° latitude centered on the Gale crater landing site. The *blue*, *orange*, *green*, and *purple* dots correspond respectively to MY24 through MY27. (**b**) MGS-TES measurements of ∼2 pm and ∼2 am ground temperatures, similar to (**a**). The *black circles* mark the minimum (0600 hr) and maximum (1300 hr) temperatures at $L_s = 0°$ averaged over the area within the landing ellipse, as predicted using data from ODY-THEMIS image I0350002. The *black lines* show the range of temperatures predicted from ODY-THEMIS within the landing ellipse at each of those times. *Grey lines* show the minimum and maximum temperatures from the JPL 1-D model

Figure 25 compares over three years (MY24-27) of MGS-TES ground temperature measurements with our model predictions. The model parameters we used result in profiles of diurnal minimum and maximum temperature that closely follow the orbital observations in an average sense. The measurements (with a footprint of a few km and sampled over a 4° longitude by 2° latitude box centered on the Gale crater landing site) capture the spatial variability of ground temperature and the influence of seasonal dust events. The former results in an envelope of ±10 °C around our predictions (occasionally even more), while the latter is especially apparent in MY25, when a planet-encircling dust storm began at $L_s = 185°$ (Smith et al. 2002). During the peak of atmospheric dust loading near $L_s = 200–210°$, the diurnal range in ground temperature decreased from ∼80 °C to only ∼30 °C.

The ODY-THEMIS instrument provides thermal maps of the landing sites with ∼100-m spatial resolution, especially useful for understanding how the thermal environment may change over the course of the rover's traverse. At Gale crater, thermal inertia varies significantly over the landing ellipse and the central mound (Fergason et al. 2012). We have used the data and numerical thermal model described by Fergason et al. (2012, 2006) to create
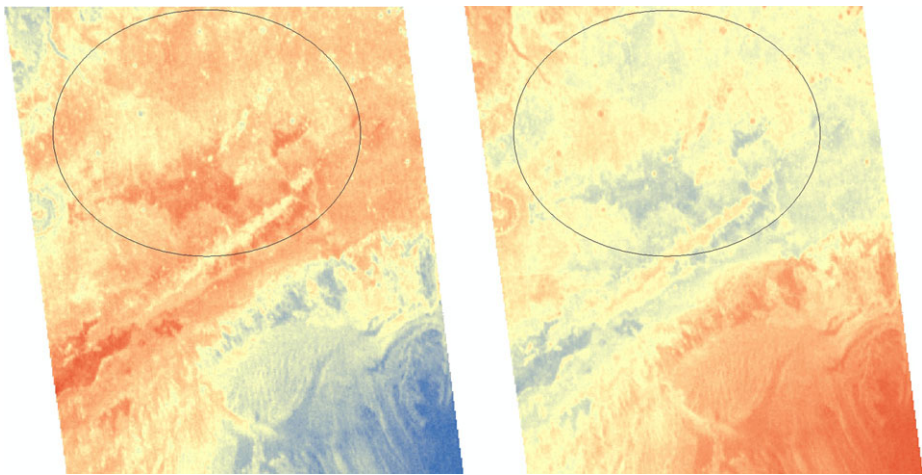
Fig. 26 Predicted temperature maps for the Gale crater 25 × 20-km landing ellipse and lower portions of its central mound at $L_s = 0°$, and at 0600 hr (*left*) and 1300 hr (*right*). The left map is linearly stretched from −100 °C (*blue*) to −60 °C (*red*). The right map is stretched from −30 °C to +15 °C. *Both maps* are derived from ODY-THEMIS image I0350002 acquired at $L_s = 353°$ and 0312 hr

predicted diurnal minimum and maximum temperature maps at various seasonal points at Gale crater (Fig. 26). At each pixel of a temperature image acquired near in local time and season to the desired prediction, a thermal model is used to derive a thermal inertia. The results are used with the model to create predicted temperature maps at arbitrary times/seasons. The results for Gale crater at $L_s = 0°$ also are plotted on Fig. 25, showing a favorable comparison with the lower-resolution MGS-TES data and the other model predictions.

The rover's operations degrade primarily with colder temperatures. The summers at the higher-latitude, southern-hemisphere sites would have provided the most efficient operations environment (i.e., least electrical heating required), but their cold and long winters more than remove this benefit when integrated over a Mars year. Mawrth Vallis and Gale crater provide an operations environment that is less variable throughout the year, though always slightly degraded, with Mawrth Vallis' shorter winter giving it a slight overall advantage. At Gale crater, we expect to use some electrical heating throughout the year, with winters requiring significant heating durations and energy. However, we do not anticipate periods of "hibernation" when no operations are possible.

7 Summary

This paper has described the atmospheric characterization program used to help certify that the MSL EDL system is capable of safely landing the 900-kg Curiosity rover at the plains of Gale crater on August 6, 2012. It also describes the characterization of the environment that the rover must operate within during its prime mission of one Mars year. Both assessments were carried out in parallel with the design and development of the landing system and rover. This led to a fluid interaction between the science and engineering teams, with the definition of environmental bounds and spacecraft capabilities evolving together, and in response to one another, especially at the detailed level.

Major architectural decisions (e.g., the sky crane, the rover) were made early on, based primarily on non-environmental factors, such as rover mass, payload and science requirements, mass efficiency, and touchdown stability. Likewise, site selection began with some general bounds (e.g., altitude, latitude) largely unconstrained by the engineering design. But as spacecraft development progressed and performance became better known, and as landing sites were scientifically studied in more detail with existing orbiters, trades could be made across the entire system in order to maximize both safety and science value. Further, the design margins within the EDL system and rover could be optimized based on where the greatest threats were found, and reduced in other areas. As an example, the large number of scientifically interesting sites at low elevations allowed an early design requirement on elevation to be relaxed. This, in turn, allowed that design margin to be partially shifted toward extra robustness to winds and dust events at lower-elevation sites. Surface environment studies allowed the rover design teams and science team to jointly make trades between latitude (i.e., colder winter temperatures) and factors such as rover productivity, battery size, energy usage for heating vs. science, etc. The positive outcome of this multi-year process was a final site safety certification that was nearly a non-event; the four finalist sites, all of premier scientific value, were all judged to pose acceptable risk to a safe landing and to safe and productive surface operations.

References

C.H. Acton, Planet. Space Sci. **44**, 65 (1996)

M. Allison, M. McEwen, Planet. Space Sci. **48**, 215 (2000)

J.R. Barnes, D. Tyler, in *Seventh International Conference on Mars, Abstract #3094* (Lunar and Planetary Institute, Houston, 2007) (CD-ROM)

B.P. Briegleb, J. Geophys. Res. **97**, 7603 (1992)

A. Chen, A. Vasavada, A. Cianciolo, J. Barnes, D. Tyler, S. Rafkin, D. Hinson, S. Lewis, in *IEEE Aerospace Conference Proceedings* (2010). doi:10.1109/AERO.2010.5447015

A.D. Cianciolo, D.W. Way, R.W. Powell, in *AIAA/AAS Astrodynamics Specialist Conference and Exhibit, AIAA-2008-6472* (2008a)

A.D. Cianciolo, D.W. Way, R.W. Powell, A. Chen, in *Third International Workshop on the Mars Atmosphere* (2008b), p. 9039

R.T. Clancy, M.J. Wolff, P.R. Christensen, J. Geophys. Res. (2003). doi:10.1029/2003JE002058

B.J. Conrath, Icarus **24**, 36–46 (1975)

B.J. Conrath, J.C. Pearl, M.D. Smith, W.C. Maguire, P.R. Christensen, S. Dason, M.S. Kaelberer, J. Geophys. Res. **105**, 9509 (2000)

R.L. Fergason, P.R. Christensen, H.H. Kieffer, J. Geophys. Res. (2006). doi:10.1029/2006JE002735

R.L. Fergason, P.R. Christensen, M.P. Golombek, T.J. Parker, Space Sci. Rev. (2012). doi:10.1007/s11214-012-9891-3

F. Forget, F. Hourdin, R. Fournier, C. Hourdin, O. Talagrand, M. Collins, S.R. Lewis, P.L. Read, J.-P. Huot, J. Geophys. Res. **104**, 24,155 (1999)

F. Forget, A. Spiga, B. Dolla, S. Vinatier, R. Melchiorri, P. Drossart, A. Gendrin, J.-P. Bibring, Y. Langevin, B. Gondet, J. Geophys. Res. (2007). doi:10.1029/2006JE002871

M.P. Golombek, J.A. Grant, T.J. Parker, D.M. Kass, J.A. Crisp, S.W. Squyres, A.F.C. Haldemann, M. Adler, W.J. Lee, N.T. Bridges, R.E. Arvidson, M.H. Carr, R.L. Kirk, P.C. Knocke, R.B. Roncoli, C.M. Weitz, J.T. Schofield, R.W. Zurek, P.R. Christensen, R.L. Fergason, F.S. Anderson, J.W. Rice, J. Geophys. Res. (2003). doi:10.1029/2003JE002074

M.P. Golombek et al., Space Sci. Rev. (2012, this issue)

J.A. Grant, M.P. Golombek, J.P. Grotzinger, S.A. Wilson, M.M. Watkins, A.R. Vasavada, J.L. Griffes, T.J. Parker, Planet. Space Sci. (2011). doi:10.1016/j.pss.2010.06.016

G.A. Grell, J. Dudhia, D.R. Stauffer, A description of the fifth-generation Penn-State/NCAR mesoscale model (MM5). NCAR Tech. Note NCAR/TN-398+, STR, Natl. Cent. for Atmos. Res., Boulder, Colo (1994)

J. Grotzinger, Nat. Geosci. (2009). doi:10.1038/ngeo480

J.P. Grotzinger et al., Space Sci. Rev. (2012, this issue)

R.M. Haberle, M.M. Joshi, J.R. Murphy, J.R. Barnes, J.T. Schofield, G. Wilson, M. Lopez-Valverde, J.L. Hollingsworth, A.F.C. Bridger, J. Schaffer, J. Geophys. Res. **104**, 8957 (1999)

R. Haberle, J.B. Pollack, J.R. Barnes, R.W. Zurek, C.B. Leovy, J.R. Murphy, H. Lee, J. Schaeffer, J. Geophys. Res. (1993a). doi:10.1029/92JE02946

R.M. Haberle, H.C. Houben, R. Hertenstein, T. Herdtle, J. Atmos. Sci. **50**, 1544 (1993b)

R.M. Haberle, J.R. Barnes, J.R. Murphy, M.M. Joshi, J. Schaeffer, J. Geophys. Res. **102**, 13301 (1997)

R.M. Haberle, M.M. Joshi, J.R. Murphy, J.R. Barnes, J.T. Schofield, G. Wilson, M. Lopez-Valverde, J.L. Hollingsworth, A.F.C. Bridger, J. Schaffer, J. Geophys. Res. **104**, 8957 (1999)

N.G. Heavens, D.J. McCleese, M.I. Richardson, D.M. Kass, A. Kleinböhl, J.T. Schofield, J. Geophys. Res. (2011). doi:10.1029/2010JE003713

S.L. Hess, J.A. Ryan, J.E. Tillman, R.M. Henry, C.B. Leovy, Geophys. Res. Lett. **7**, 197 (1980)

B.B. Hicks, Q. J. R. Meteorol. Soc. **102**, 535 (1976)

D.P. Hinson, M. Pätzold, S. Tellmann, B. Häusler, G.L. Tyler, Icarus (2008). doi:10.1016/j.icarus. 2008.07.003

D.P. Hinson, R.A. Simpson, J.D. Twicken, G.L. Tyler, F.M. Flasar, J. Geophys. Res. **104**, 26997 (1999)

D.P. Hinson, R.J. Wilson, J. Geophys. Res. (2004). doi:10.1029/2003JE002129

D.P. Hinson, M. Patzold, S. Tellmann, B. Hausler, G.L. Tyler, Icarus **198**, 57 (2008)

F. Hourdin, J. Geophys. Res. **97**, 18,319 (1992)

F. Hourdin, F. Forget, O. Talagrand, J. Geophys. Res. **100**, 5501 (1995)

J.H. Joseph, W.J. Wiscombe, J.A. Weinman, J. Atmos. Sci. **33**, 2452 (1976)

C.G. Justus, B.F. James, S.W. Bougher, A.F.C. Bridger, R.M. Haberle, J.R. Murphy, S. Engel, Adv. Space Res. (2002). doi:10.1016/S0273-1177(01)00569-5

C.G. Justus, A. Duvall, D.L. Johnson, Adv. Space Res. (2004). doi:10.1016/j.asr.2003.08.077

C.G. Justus, A.L. Duvall, D.L. Johnson, Adv. Space Res. (2005). doi:10.1016/j.asr.2003.02.044

M.A. Kahre, J.R. Murphy, R.M. Haberle, J. Geophys. Res. (2006). doi:10.1029/2005JE002588

D.M. Kass, T. Schofield, T.I. Michaels, S.C. Rafkin, M.I. Richardson, A.D. Toigo, J. Geophys. Res. **108**, 8090 (2003)

W. Lahoz, B. Khattatov, R. Menard (eds.), *Data Assimilation: Making Sense of Observations* (Springer, Berlin, 2010)

M.J. Ledlow, J.O. Burns, G.R. Gisler, J. Zhao, M. Zeilik, D.N. Baker, Astrophys. J. **348**, 640 (1992)

S.R. Lewis, P.L. Read, J. Geophys. Res. **108**, 15 (2003)

S.R. Lewis, P.R. Barker, Adv. Space Res. **36**, 2162 (2005)

S.R. Lewis, P.L. Read, B.J. Conrath, J.C. Pearl, M.D. Smith, Icarus **192**, 327 (2007)

S.R. Lewis, M. Collins, P.L. Read, F. Forget, F. Hourdin, R. Fournier, C. Hourdin, O. Talagrand, J.P. Huot, J. Geophys. Res. **104**, 24177 (1999)

A.C. Lorenc, R.S. Bell, B. Macpherson, Q. J. R. Meteorol. Soc. **117**, 59 (1991)

O. Martinez-Alvarado, L. Montabone, S.R. Lewis, P.L. Read, I.M. Moroz, Ann. Geophys. **27**, 3663 (2009)

D.J. McCleese, J.T. Schofield, F.W. Taylor, W.A. Abdou, O. Aharonson, D. Banfield, S.B. Calcutt, N.G. Heavens, P.G.J. Irwin, D.M. Kass, A. Kleinböhl, W.G. Lawson, C.B. Leovy, S.R. Lewis, D.A. Paige, P.L. Read, M.I. Richardson, N. Teanby, R.W. Zurek, Nat. Geosci. (2008). doi:10.1038/ngeo332

D.J. McCleese, N.G. Heavens, J.T. Schofield, W.A. Abdou, J.L. Bandfield, S.B. Calcutt, P.G.J. Irwin, D.M. Kass, A. Kleinböehl, C.B. Leovy, S.R. Lewis, D.A. Paige, P.L. Read, M.I. Richardson, J.H. Shirley, F.W. Taylor, N. Teanby, R.W. Zurek, J. Geophys. Res. (2010). doi:10.1029/2010JE003677

T.Z. Martin, N.T. Bridges, J.R. Murphy, J. Geophys. Res. (2003). doi:10.1029/2003JE002063

M.T. Mellon, B.M. Jakosky, H.H. Kieffer, P.R. Christensen, Icarus **148**, 437 (2000)

T.I. Michaels, Geophys. Res. Lett. **33**, L19S08 (2006)

T.I. Michaels, S.C.R. Rafkin, Q. J. R. Meteorol. Soc. **130**, 1251 (2004)

T.I. Michaels, S.C.R. Rafkin, J. Geophys. Res. (2008). doi:10.1029/2007JE003013

L. Montabone, S.R. Lewis, P.L. Read, D.P. Hinson, Icarus **185**, 113 (2006)

D.A. Paige, J.E. Bachman, K.D. Keegan, J. Geophys. Res. **99**, 25,959 (1994)

R.A. Pielke, W.R. Cotton, R.L. Walko, J. Tremback, W.A. Lyons, L.D. Grasso, M.E. Nicholls, M.D. Moran, D.A. Wesley, T.J. Lee, J.H. Copeland, Meteorol. Atmos. Phys. (1992). doi:10.1007/BF01025401

J.B. Pollack, M.E. Ockert-Bell, M.K. Shepard, J. Geophys. Res. **100**, 5235 (1995)

J.B. Pollack, R.M. Haberle, J. Schaeffer, H. Lee, J. Geophys. Res. **95**, 1447 (1990)

R. Prakash, P.D. Burkhart, A. Chen, K. Comeaux, C.S. Guernsey, D.M. Kipp, L.V. Lorenzoni, G.F. Mendeck, R.W. Powell, T.P. Rivellini, A.M. San Martin, S.W. Sell, A.D. Steltzner, D.W. Way, in *2008 IEEE Aerospace Conference Proceedings* (2008). doi:10.1109/AERO.2008.4526283

S.C.R. Rafkin, J. Geophys. Res. (2009). doi:10.1029/2008JE003217

S.C.R. Rafkin, Planet. Space Sci. (2011). doi:10.1016/j.pss.2011.07.015

S.C.R. Rafkin, T.I. Michaels, J. Geophys. Res. **108**, 8091 (2003)

S.C.R. Rafkin, R.M. Haberle, T.I. Michaels, Icarus **151**, 228 (2001)

S.C.R. Rafkin, M.R.V.S. Maria, T.I. Michaels, Nature **419**, 697 (2002)

S.C.R. Rafkin, T.I. Michaels, R.M. Haberle, Geophys. Res. Lett. **31**, L01703 (2004)

P. Rogberg, P.L. Read, S.R. Lewis, L. Montabone, Q. J. R. Meteorol. Soc. **136**, 1614 (2010)

M.R.V.S. Maria, S.C.R. Rafkin, T.I. Michaels, Icarus **185**, 383 (2006)

M.D. Smith, J.C. Pearl, B.J. Conrath, P.R. Christensen, J. Geophys. Res. **105**, 9539 (2000)

M.D. Smith, J.C. Pearl, B.J. Conrath, P.R. Christensen, J. Geophys. Res. **106**, 23929 (2001)

M.D. Smith, B.J. Conrath, J.C. Pearl, P.R. Christensen, Icarus **157**, 259 (2002)

M.D. Smith, Icarus **167**, 148 (2004)

A. Spiga, F. Forget, S.R. Lewis, D.P. Hinson, Q. J. R. Meteorol. Soc. **136**, 414 (2010)

J.L. Sutton, C.B. Leovy, J.E. Tillman, J. Atmos. Sci. **35**, 2346 (1978)

L.K. Tamppari, J. Barnes, E. Bonfiglio, B. Cantor, J.A. Friedson, A. Ghosh, M.R. Grover, D. Kass, T.Z. Martin, M. Mellon, T. Michaels, J. Murphy, S.C.R. Rafkin, M.D. Smith, G. Tsuyuki, D. Tyler, M. Wolff, J. Geophys. Res. (2008). doi:10.1029/2007JE003034

T.N. Titus, *Mars Polar Cap Edges Tracked over 3 Full Mars Years, 36th LPSC, 3/14-3/18, League City, TX, #1993* (2005)

A.D. Toigo, M.I. Richardson, J. Geophys. Res. **108**, 8092 (2003)

M.G. Tomaskso, L.R. Doose, M. Lemmon, P.H. Smith, E. Wegryn, J. Geophys. Res. **104**, 8987 (1999)

O.B. Toon, C.P. McKay, T.P. Ackerman, K. Santhanam, J. Geophys. Res. (1989). doi:10.1029/JD094iD13p16287

G.T. Tsuyuki, L.K. Tamppari, T.Z. Martin, J.R. Murphy, in *SAE Int. Conf. on Env. Syst.* (2007). doi:10.4271/2007-01-3239

D. Tyler, J.R. Barnes, R.M. Haberle, J. Geophys. Res. (2002). doi:10.1029/2001JE001618

D. Tyler, J.R. Barnes, J. Geophys. Res. (2005). doi:10.1029/2004JE002356

D. Tyler, J.R. Barnes, E.D. Skyllingstad, J. Geophys. Res. (2008). doi:10.1029/2007JE003012

R.J. Wilson, S.R. Lewis, L. Montabone, M.D. Smith, Geophys. Res. Lett. **35**, L07202 (2008)

P. Withers, Space Sci. Rev. (2012). doi:10.1007/s11214-012-9876-2

M.J. Wolff, R.T. Clancy, J. Geophys. Res. (2003). doi:10.1029/2003JE002057